NASA TECHNICAL NOTE

NASA TN D-7710

NASA TN D-7710

INVESTIGATION OF NEW RADAR-DATA-REDUCTION TECHNIQUES USED TO DETERMINE DRAG CHARACTERISTICS OF A FREE-FLIGHT VEHICLE

by Gerard E. Woodbury and John W. Wallace

Langley Research Center
Hampton, Va. 23665

NATIONAL AERONAUTICS AND SPACE ADMINISTRATION • WASHINGTON, D. C. • OCTOBER 1974

1. Report No.	2. Government Accession No.	3. Recipient's Catalog No.
NASA TN D-7710		

4. Title and Subtitle	5. Report Date
INVESTIGATION OF NEW RADAR-DATA-REDUCTION TECHNIQUES USED TO DETERMINE DRAG CHARACTERISTICS OF A FREE-FLIGHT VEHICLE	October 1974
	6. Performing Organization Code

7. Author(s)	8. Performing Organization Report No.
Gerard E. Woodbury and John W. Wallace	L-8398
	10. Work Unit No. 502-27-01-01

9. Performing Organization Name and Address	11. Contract or Grant No.
NASA Langley Research Center Hampton, Va. 23665	
	13. Type of Report and Period Covered
12. Sponsoring Agency Name and Address	Technical Note
National Aeronautics and Space Administration Washington, D.C. 20546	14. Sponsoring Agency Code

15. Supplementary Notes

16. Abstract

An investigation was conducted of new techniques used to determine the complete transonic drag characteristics of a series of free-flight drop-test models using principally radar tracking data. The full capabilities of the radar tracking and meteorological measurement systems were utilized. In addition, preflight trajectory design, exact kinematic equations, and visual-analytical filtering procedures were employed. The results of this study were compared with the results obtained from analysis of the onboard, accelerometer and pressure sensor data of the only drop-test model that was instrumented. The accelerometer-pressure drag curve was approximated by the radar-data drag curve. However, a small amplitude oscillation on the latter curve precluded a precise definition of its drag rise.

17. Key Words (Suggested by Author(s))	18. Distribution Statement
Visual spline-function filtering New radar-determined drag Hand-calculated drag Kalman-filter comparison	Unclassified – Unlimited STAR Category 30

19. Security Classif. (of this report)	20. Security Classif. (of this page)	21. No. of Pages	22. Price*
Unclassified	Unclassified	48	$3.25

*For sale by the National Technical Information Service, Springfield, Virginia 22151

INVESTIGATION OF NEW RADAR-DATA-REDUCTION TECHNIQUES USED TO DETERMINE DRAG CHARACTERISTICS OF A FREE-FLIGHT VEHICLE

By Gerard E. Woodbury and John W. Wallace
Langley Research Center

SUMMARY

An investigation was conducted of new techniques used to determine the complete transonic drag characteristics of a series of free-flight drop-test models from principally radar tracking data. In addition to fully using the capabilities of both the tracking radars and the meteorological measurement systems, preflight trajectory design, exact kinematic equations, and visual-analytical filtering techniques were employed in the study. The results of this endeavor were compared with the results obtained from analysis of the onboard, accelerometer and pressure sensor data of the only drop-test model that was instrumented.

The accelerometer drag curve was approximated by the radar-data-alone drag curve. However, white noise in the radar data prevents a precise definition of the drag rise. As a backup method, on the other hand, the radar-data-alone approach has considerable merit for estimating drag rise, particularly if subsonic wind-tunnel data are coupled with the flight data.

INTRODUCTION

A series of free-flight drop tests was conducted by the NASA Langley Research Center to determine the transonic drag characteristics of a low-drag supercritical body of revolution. The drop-test series consisted of three uninstrumented models and one instrumented model. The instrumented model contained longitudinal accelerometers and various pressure sensors. These instruments were the primary source of data for the determination of the drag of the test configuration. The free-flight drag characteristics obtained from analysis of these data are presented in reference 1.

In the planning stages of the test program, meanwhile, it was felt that while the instrumented model was being readied, three uninstrumented models could be quickly constructed, aircraft dropped, and tracked by radars. By using the radar-data reduction methods of the past, these uninstrumented drop tests could provide a quick look at the

free-flight subsonic and supersonic levels of drag. The tests could also help perfect the aircraft-drop and radar-tracking techniques; furthermore, in the event of a malfunction of the instrumented model, they could also possibly serve as a backup for the determination of the drag rise. It was later decided to explore this latter possibility more thoroughly when, as a result of a stringent accuracy requirement placed on the test series, much emphasis was put on using the full capabilities of the tracking radars and the meteorological measurement systems. This emphasis coincidentally increased the chances of successfully determining the complete transonic drag characteristics of the model from radar data alone.

The purpose of this report is to present the new techniques devised for this effort and the results of the application of these techniques to the radar data of the drop-test series. The approach taken in this work involved: (1) updating the equations for determining the drag from good approximations to more exact expressions written in a form conducive to accurate smoothing of the data, (2) using a smoothing technique new to this field of endeavor and using it in conjunction with a visual display in order to assure physical relevance, (3) designing the flight trajectory to maximize the contribution of data known to be the most accurate, and (4) employing the most recently developed meteorological measurement systems.

SYMBOLS

C_D drag force coefficient, $\frac{D}{q_\infty S}$

C_T total aerodynamic force coefficient; for small angles of attack $C_T \approx C_D \approx C_X$

C_X axial-force coefficient

d_b base diameter of flight vehicle, cm

d_{max} maximum diameter of flight vehicle, cm

D drag force, N

$F_I^A(O)_I$ total aerodynamic force relative to Earth-centered inertial axis system, N (see ref. 2)

g sea-level acceleration of gravity, m/sec^2

h geodetic height of flight vehicle, m

m	mass of flight vehicle, kg
M	Mach number
q_∞	free-stream dynamic pressure, N/m^2
R	flat-Earth horizontal range, m
S	reference area, m^2
t	elapsed flight time, sec
V_c	atmospheric speed of sound, m/sec
V_E	magnitude of Earth-relative velocity of flight vehicle, m/sec
V_W	magnitude of wind velocity, m/sec
V_∞	magnitude of free-stream velocity of flight vehicle, m/sec
W	weight of flight vehicle, mg, N
x	north-south component of R, m
y	east-west component of R, m
$\gamma_{E,p}$	Earth-relative flight-path angle in vertical plane, deg
$\gamma_{E,y}$	Earth-relative flight-path angle in horizontal plane, deg
η	total angle of attack, deg
θ_r	elevation angle measured by radar above its horizontal plane, deg
ρ	slant range measured by radar in line of sight to flight vehicle, m
$\dot{\rho}$	rate of change of slant range, m/sec

$\dot{\rho}_D$ $\dot{\rho}$ measured directly by the radar operating in Doppler mode, m/sec

ρ_∞ free-stream density of atmosphere, kg/m^3

ψ_r azimuth angle measured from north by radar in its horizontal plane, deg

ψ_w wind azimuth, referenced to north, deg

A dot over a symbol denotes differentiation with respect to time; a double dot over a symbol denotes a second differentiation with respect to time.

ANALYTICAL METHODS

General

A review of the method typically used in the past for obtaining C_D from radar data alone was made. It was found that this technique had been devised in the days before high-speed computers and was initially set up to be done primarily by hand and had necessarily used many simplifying assumptions. These assumptions are presented in appendix A together with the equations based on them for determining C_D. Although most of the handwork was in time eliminated from the past method by one means or another, its equations changed little or not at all. Because of a stringent accuracy requirement, preflight calculations were made to check the accuracy of the equations when applied to this particular test series. Using the drag-force equation (A1) with a computer-generated nominal trajectory of the test configuration, a 3-percent error in C_D was found in the test region of interest. Thus, it was deemed necessary to devise new formulations which are physically more exact than the old ones and to make use of the latest technology and equipment. The new radar-data-reduction technique presented herein employs a computerized curve-fitting program new to this work in its filtering process and uses it in conjunction with a control console. This arrangement permits, in all phases of the filtering, visual inspection of the smoothed and differentiated data; through direct access to the computer program, it also provides a more expeditious means of managing the data.

The equations for computing position, velocity, and acceleration are written in an oblate-spheroidal Earth-centered inertial frame. In addition to being more exact, these equations were specifically tailored so that the basic radar measurements $(\rho,\psi_r,\theta_r,\dot{\rho}_D)$, their time rate of change, and where applicable their second time rate of change would be input directly to determine C_D. This approach enables due regard to be given to the relative accuracy of each measurement by assuring that very accurate data would not be degraded by less accurate data in the filtering process.

Hand-Calculation Method

For convenience, the past method may also be referred to as the hand-calculation method. No one reference could be found which satisfactorily gave a complete description of its original formulation. A version of it was reconstructed, however, and is presented in appendix A along with its basic assumptions and equations. Basically, two radars were involved in the test setup. A continuous-wave Doppler radar positioned within a short distance of the launching site measured $\dot{\rho}_D$, the rate of change of slant range to the model. A remote second radar of a positional nature provided the spatial location of the model in spherical coordinates (ρ,ψ_r,θ_r). (Today's FPQ-6 radar combines both of these modes of tracking in one facility.) In general, there were two methods of launching the flight models: by rocket propulsion and by a helium gun. As the latter name implies, small models were accelerated to low supersonic speed by a controlled expansion of the gas (helium) acting on a push-plate within a 6-inch rifle barrel. The determination of the transonic drag variation was made for both launch modes in coasting flights as the models decelerated from low supersonic to high subsonic speeds.

The hand-calculation method is still applicable today. It yields its best results when applied to flight tests wherein large drag forces overshadow those forces neglected by the simplifying assumptions of the method. It was the neglect of the Coriolis force which, in fact, led to the aforementioned 3-percent error in C_D of the low drag bodies of this test series. The hand-calculation method could be particularly useful to those who are without sophisticated software and who are not laboring under the constraint of extreme accuracy as herein was the case. The hand-calculation method was updated from time to time primarily to eliminate its handwork and to adapt it to other modes of free-flight testing. The results of its application over the years to many flight test models are summarized in reference 3.

New Filtering and Data-Reduction Method

A block diagram summarizing the new procedures employed in the analysis of the flight data is shown in figure 1. The data are first smoothed (filtered) by a cubic spline approximation computer program (ref. 4) utilizing a cathode-ray tube console (CSA/CRT). On the console, the data are visually presented and checked for wild points, dropouts, and any other data anomalies. The data are then fitted to cubic equations (splines) between finite boundaries (knots). The degree to which the fit approximates the data is also checked visually on the console. The obvious advantage of this technique is that engineering judgment based on experience may be exercised at this point, and if not satisfied, iterations may be performed varying the number of splines and location of knots. The fitting equations are constrained such that the function, its first derivative,

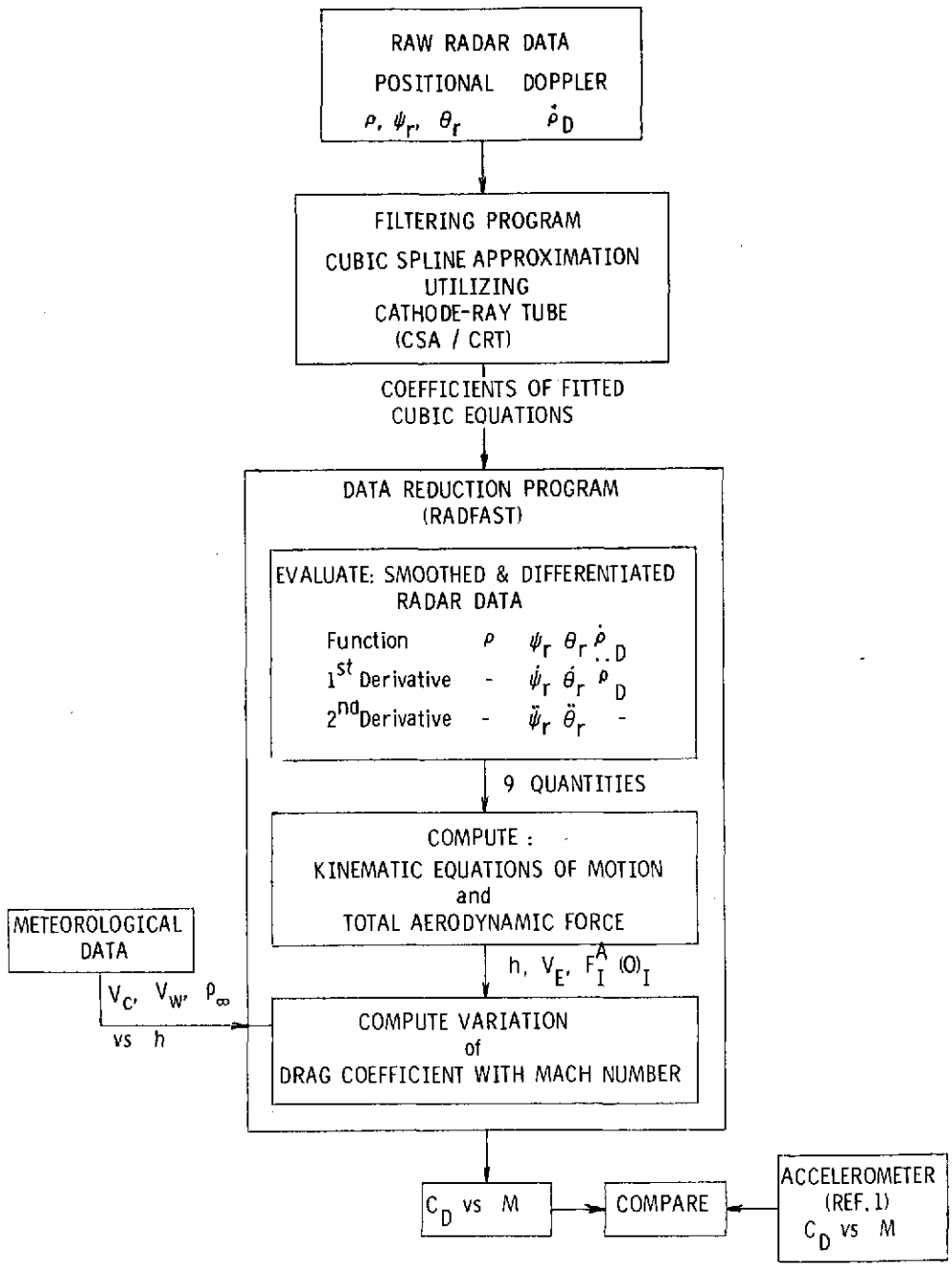

Figure 1.- Block diagram illustrating the flow of raw data to reduced coefficients.

and second derivative must be continuous at the boundaries. The first and second derivatives of the function (data) fitted by cubic equations, naturally, take the form of quadratic and linear equations, respectively. Thus, it was not surprising to find that while the derivatives were continuous at each knot, the derivative time histories were not necessarily smooth in appearance overall. This was particularly true of the second derivatives. For that reason, the internally computed first derivatives were also fitted and new first and second derivatives were obtained which were more accurate and less erratic. The effect of this successive smoothing procedure on the data and its initial first and second derivatives is illustrated more thoroughly later.

All of the equations for determining C_D from radar data alone were incorporated into a second computer program which is hereinafter referred to as RADFAST and are presented in appendix B. The output of the CSA/CRT program takes the form of coefficients of the cubic equations. This output then serves as input to RADFAST where the coefficients are used to generate time histories of the nine quantities (ρ, ψ_r, θ_r, and their first and second derivatives) that are required by the kinematic equations of RADFAST in order to determine displacements, velocities, and accelerations in an inertial axis system set in the center of a rotating oblate spheroid. The important output from the computations of the kinematic equations (eqs. (B1) to (B38) in appendix B) are:

(1) Geodetic altitude (eq. (B28)) is required to relate environmental parameters to the flight trajectory.

(2) Free-stream velocity (eq. (B36)) is obtained by adding the wind velocity vectorially to the Earth-relative velocity.

(3) Total inertial acceleration (eq. (B19)) is required in the determination of the total aerodynamic force acting on the body.

The total aerodynamic force of the body is computed by the product of the mass of the body and the total aerodynamic acceleration in equation (B43) wherein the gravitational acceleration of the body is subtracted vectorially from the total inertial acceleration determined from radar data. The total aerodynamic force coefficient of the body is computed by

$$C_T = \frac{\left|F_I^A(O)_I\right|}{q_\infty S}$$

where $q_\infty = \frac{1}{2}\rho_\infty V_\infty^2$. The results of preflight studies presented in appendix C indicated that the model could be expected to fly at very small angles of attack ($\eta \approx 0$) during the data period. Thus

$$C_D \approx C_T$$

Finally, with M found by

$$M = \frac{V_\infty}{V_c}$$

the variation of C_D with M may be determined.

APPLICATION OF TECHNIQUES TO FLIGHT TESTS

The flight test series was conducted at the NASA Wallops Flight Center. The CSA-RADFAST techniques described in the previous section were applied to the radar flight data of three of the models of the drop-test series. Although each of the three uninstrumented models (designated R1, R2, and R3) and the instrumented model (R4) were successfully dropped and radar tracked, the FPQ-6 radar was not able to obtain any Doppler data during the flight of the second model, R2. Consequently, because of the incompleteness of the data, the CSA-RADFAST techniques were not applied to the R2 flight. Since the tests were largely repetitious in nature, the atmospheric and radar flight data of only one model are presented herein and may be thought of as being typical of that of the three models analyzed.

Test Models

The four test models were bodies of revolution with identical exterior contours and were designed to have a drag divergence near Mach 1. A sketch of the model is shown in figure 2. A photograph of the model mounted on the drop aircraft is shown in figure 3. The model length was 114.3 cm and the maximum diameter was 12.7 cm. The fins were swept 45° and had biconvex cross section with a thickness-to-chord ratio of 0.03. The models were mass balanced to zero, within the tolerance of the balance machine. Each model had a mass of approximately 36.4 kg and contained a beacon to aid in radar acquisition and tracking.

Test Description

In each flight test the model was dropped from a T-33 aircraft flying horizontally with a nominal altitude of 9144 m and Earth-relative velocity of approximately 183 m/sec. The trajectory was directed at the Wallops FPQ-6 radar such that $\dot{\rho}_D$, the only velocity component measured directly and, hence, the most accurate component of the total velocity, was maximized. For the same reason the line of sight from the radar was designed to be tangent to the flight path at a point in time when $M = 1$. This design condition was not met in the actual flight tests because of Wallops range safety limits. For example, in the actual flight test of R4 at $M = 1$ the flight-path angle $\gamma_{E,p}$ was approximately -61° while the radar elevation look angle θ_r was approximately 20°.

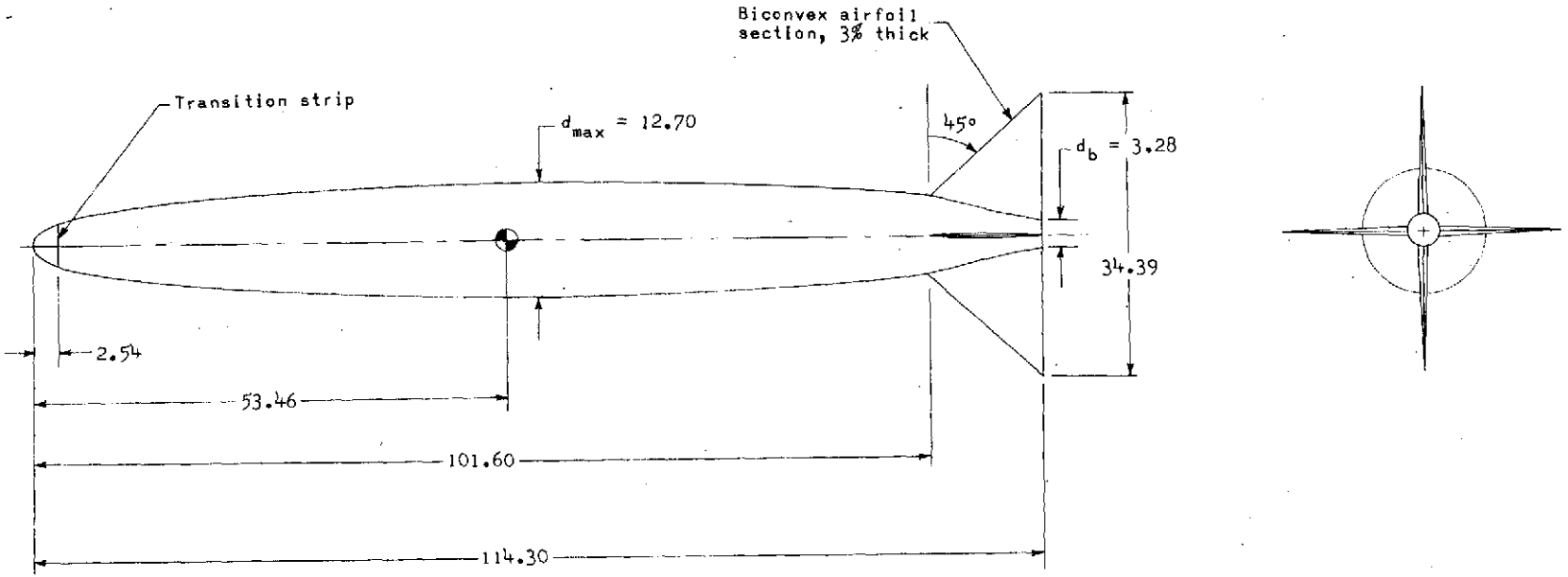

Figure 2.- Sketch of drop-test model. Dimensions are in centimeters.

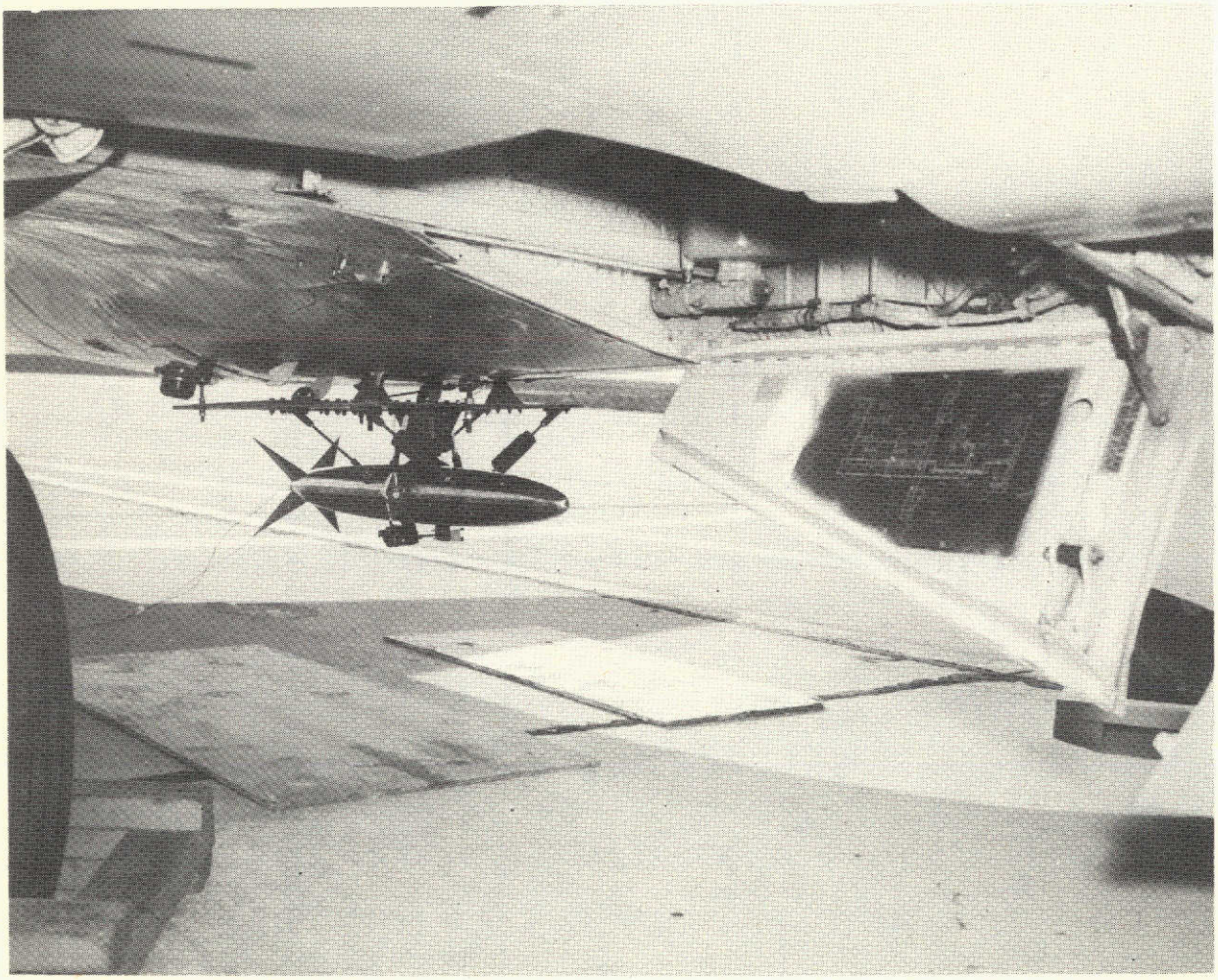

L-74-1142

Figure 3.- Photograph of flight vehicle on the launch aircraft.

Atmospheric Properties

Measurements of free-stream temperature, pressure, and relative humidity were made by rawinsondes for each flight. Free-stream density and speed of sound were derived from these measurements. The measured and subsequently derived atmospheric quantities of the R4 flight are presented in figure 4. The winds were measured by the Jimsphere technique (ref. 5). Briefly, the Jimsphere technique is a method developed for measuring winds which employs precise radar tracking of a smooth, superpressure, spherical balloon modified by the addition of conical surface-roughness elements. The winds are averaged over intervals of 25 m as opposed to approximately 300 m as is done in the commonly used radiosonde system.

Test Data

The radar data $(\rho,\psi_r,\theta_r,\dot{\rho}_D)$ measured during the flight of R4 is presented in figure 5. Superimposed on the data is the smoothing of data by the CSA/CRT technique. Using the coefficients of the cubic equations fitted to the data in a least-square sense, the first and second derivatives of the ψ_r and θ_r data were generated and are presented in figures 6 and 7, respectively. The θ_r plots are particularly illustrative of the need for the aforementioned successive smoothing. Its second derivative $\ddot{\theta}_r$ clearly shows in figure 7 that while the derivatives are continuous at each knot, their overall time history is oscillatory in nature, apparently about some mean. The dashed curves (figs. 6 and 7) represent the new first and second derivatives obtained by fitting new sets of cubic equations to the initial internally generated first derivatives of the ψ_r and θ_r data. Notice that this procedure does not appreciably change the general value of the original first derivatives but does considerably alter the time history of the second derivative to a more plausible curve. The successive smoothing procedure was only required for the ψ_r and θ_r data since the first derivative of ρ is measured directly by the radar and is the so-called Doppler velocity $\dot{\rho}_D$.

RESULTS OF APPLICATION

The results of applying the CSA-RADFAST method to the radar flight data of the test models were obtained and then compared with the results of the analysis (ref. 1) of the accelerometer and pressure sensor data of the instrumented flight model, R4. The two sets of R4 results are of particular interest, for here using different types of data from the same flight (a flight in which the model obviously flew the same trajectory, encountered the same winds, etc.) it was possible to make a one-to-one comparison of their resultant drag variations.

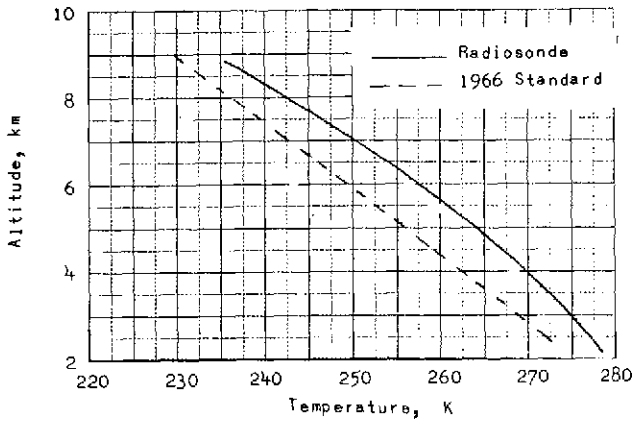

(a) Temperature.

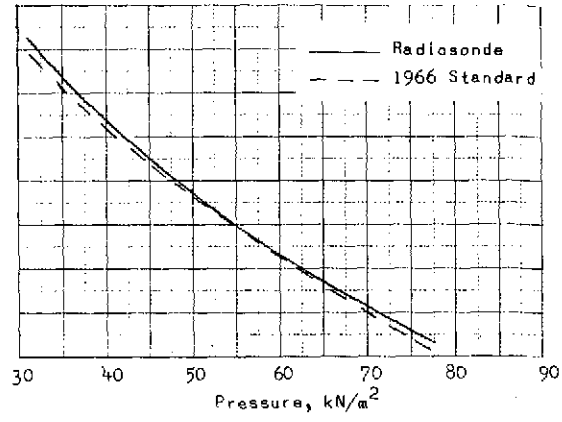

(b) Pressure.

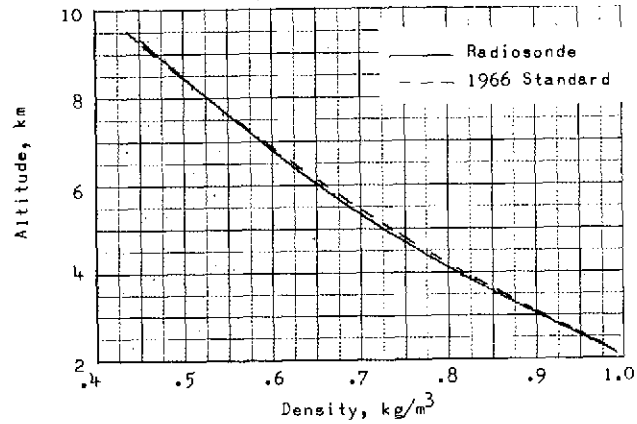

(c) Density.

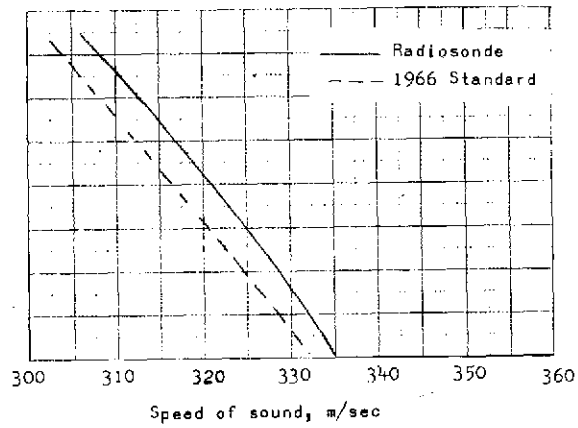

(d) Speed of sound.

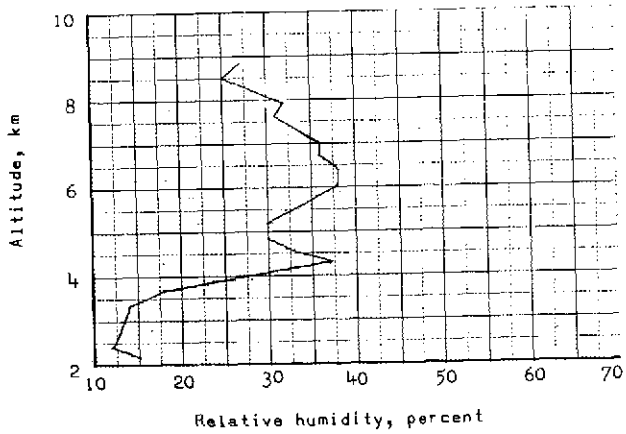

(e) Relative humidity.

Figure 4.- Meteorological data.

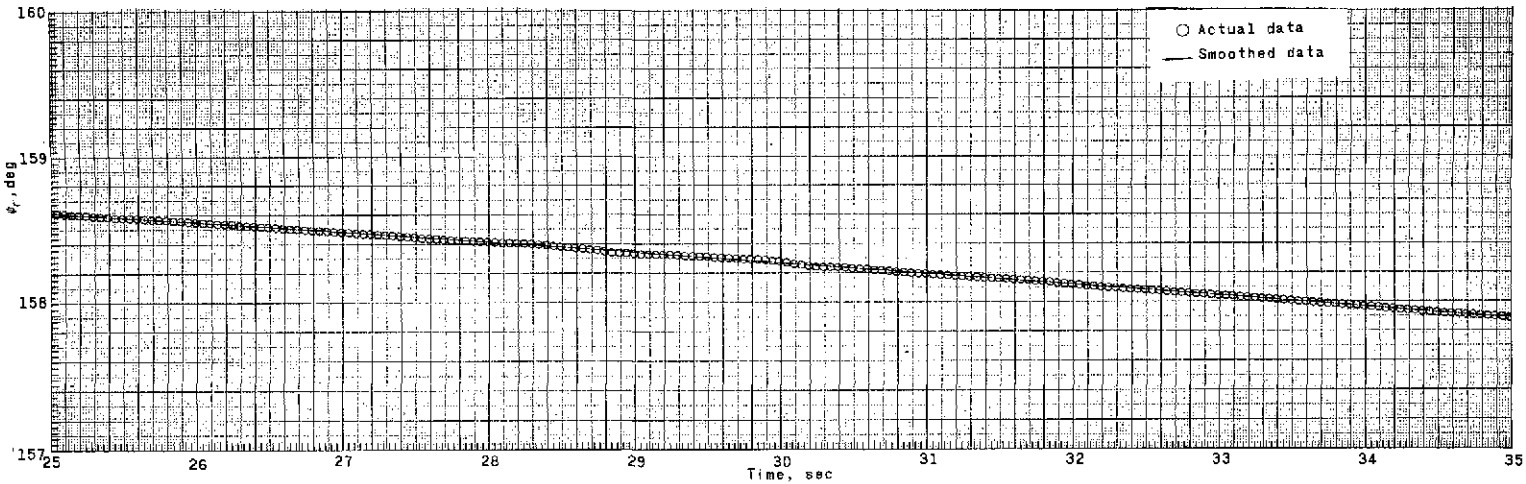

(a) Azimuth.

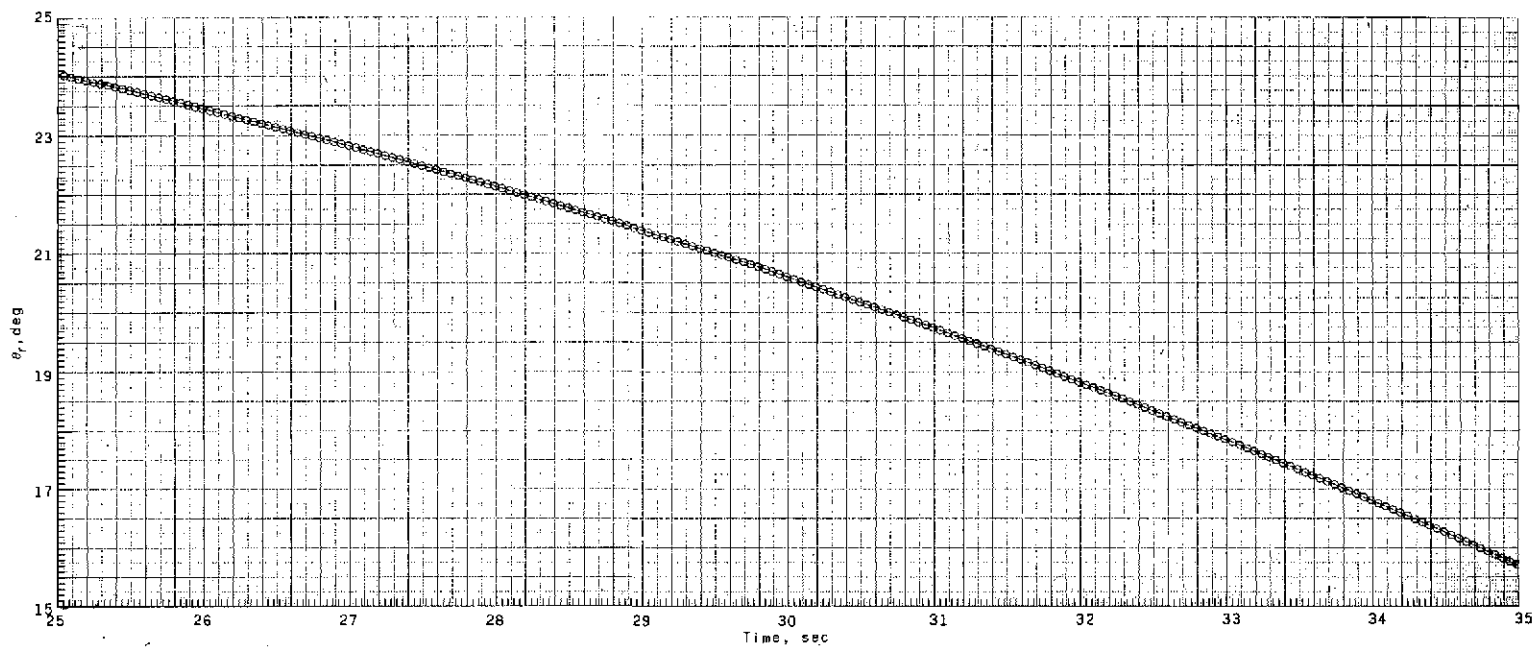

(b) Elevation.

Figure 5.- Radar flight data.

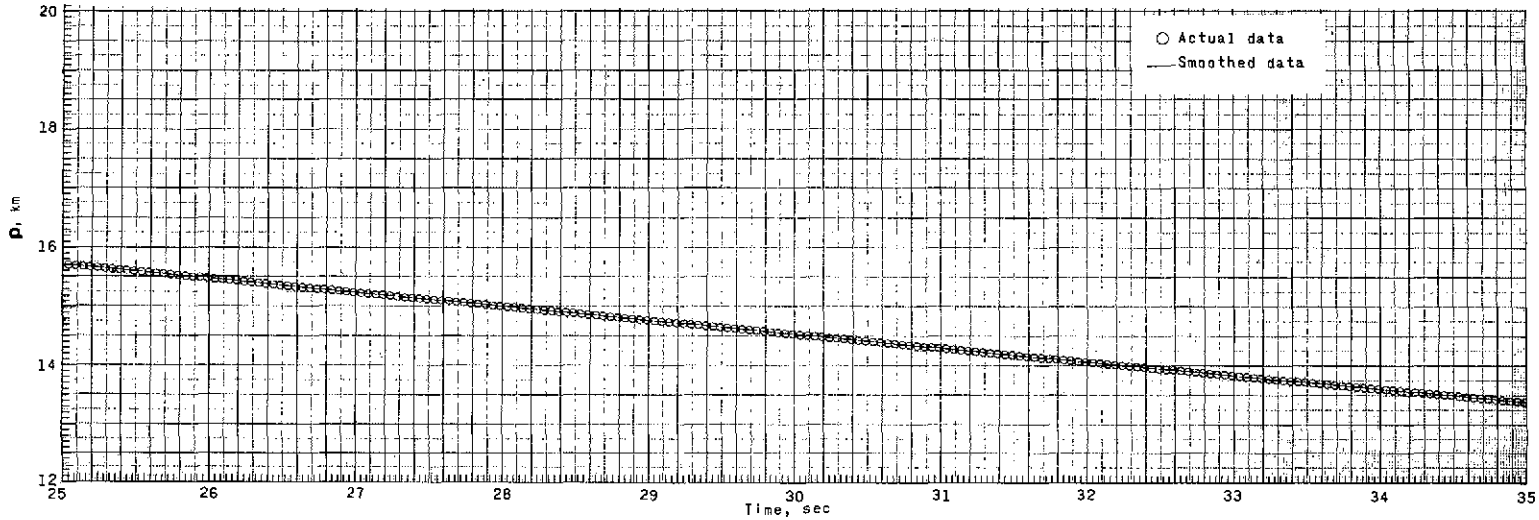

(c) Slant range.

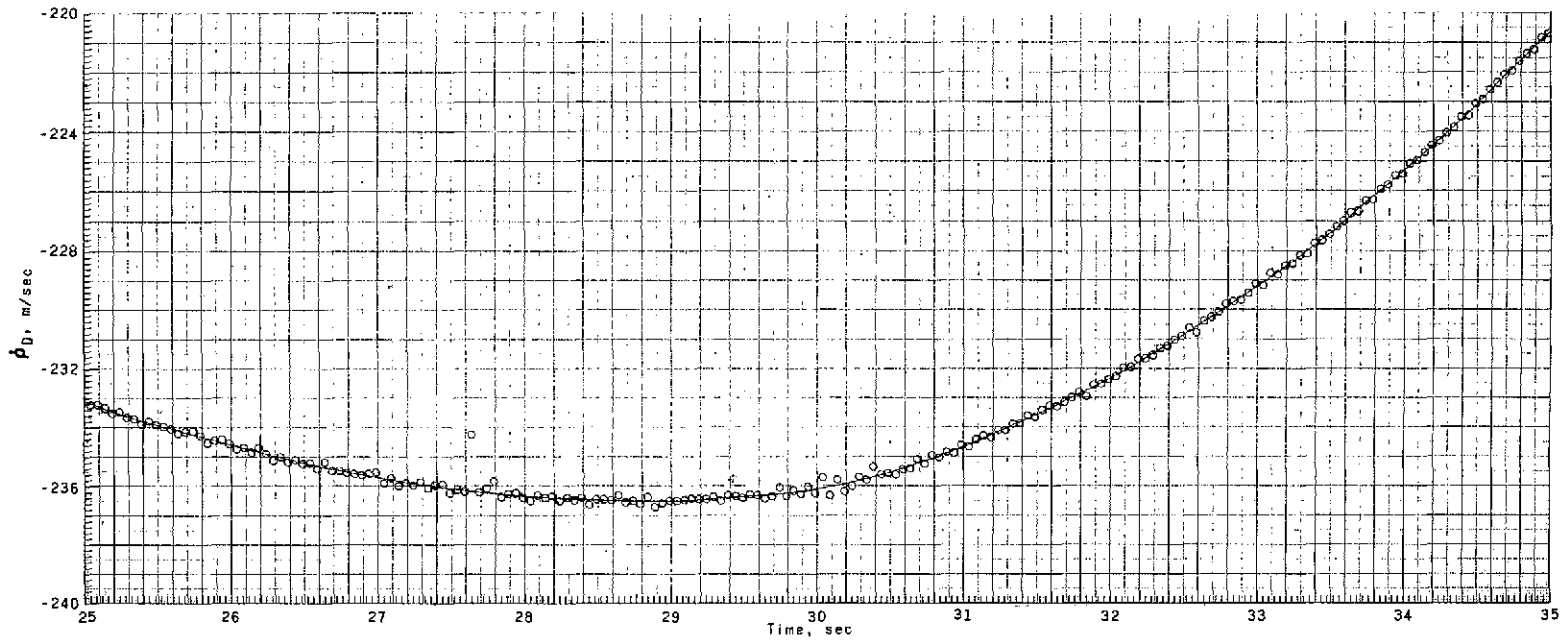

(d) Range rate.

Figure 5.- Concluded.

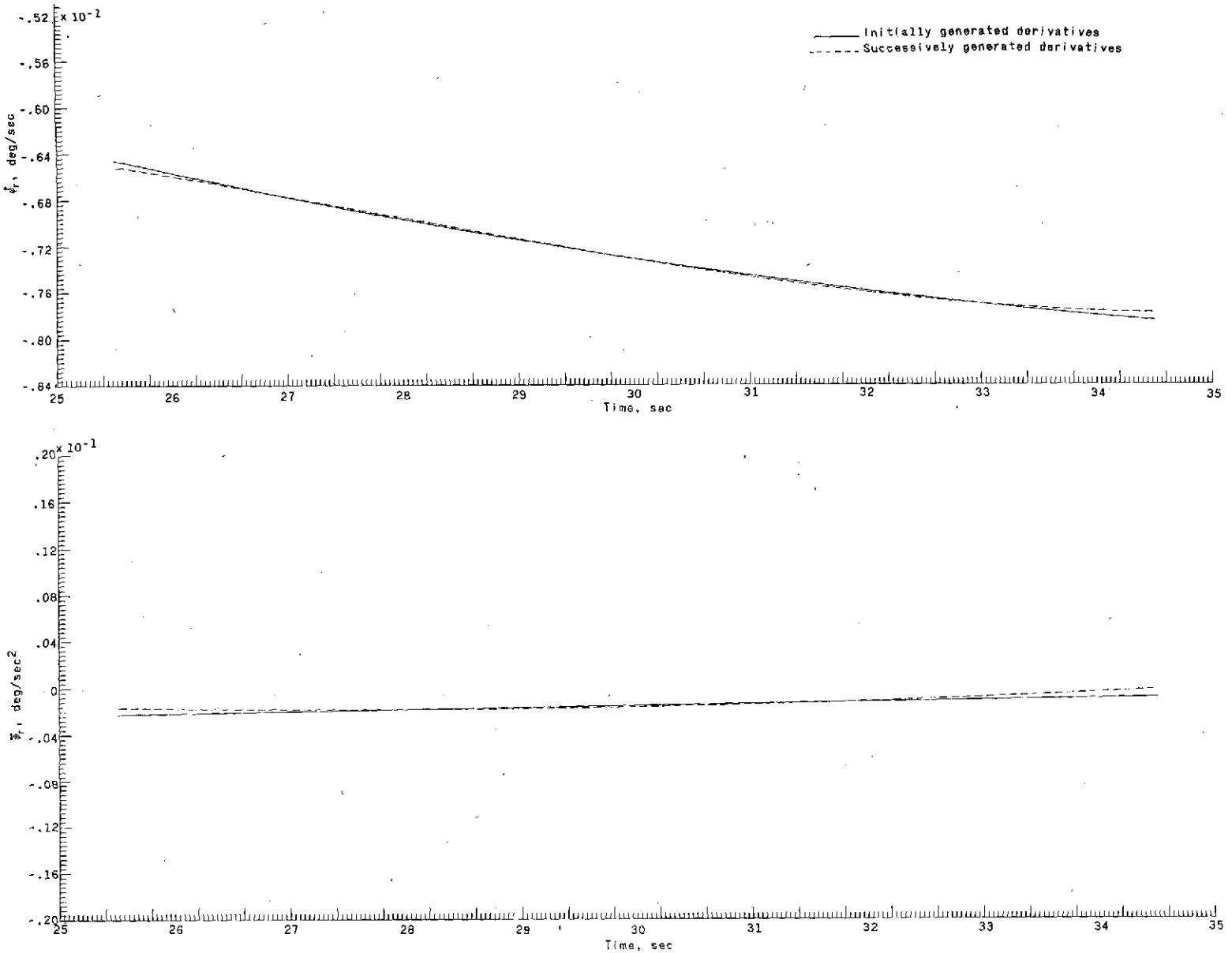

Figure 6.- Generated first and second derivatives of the azimuth data.

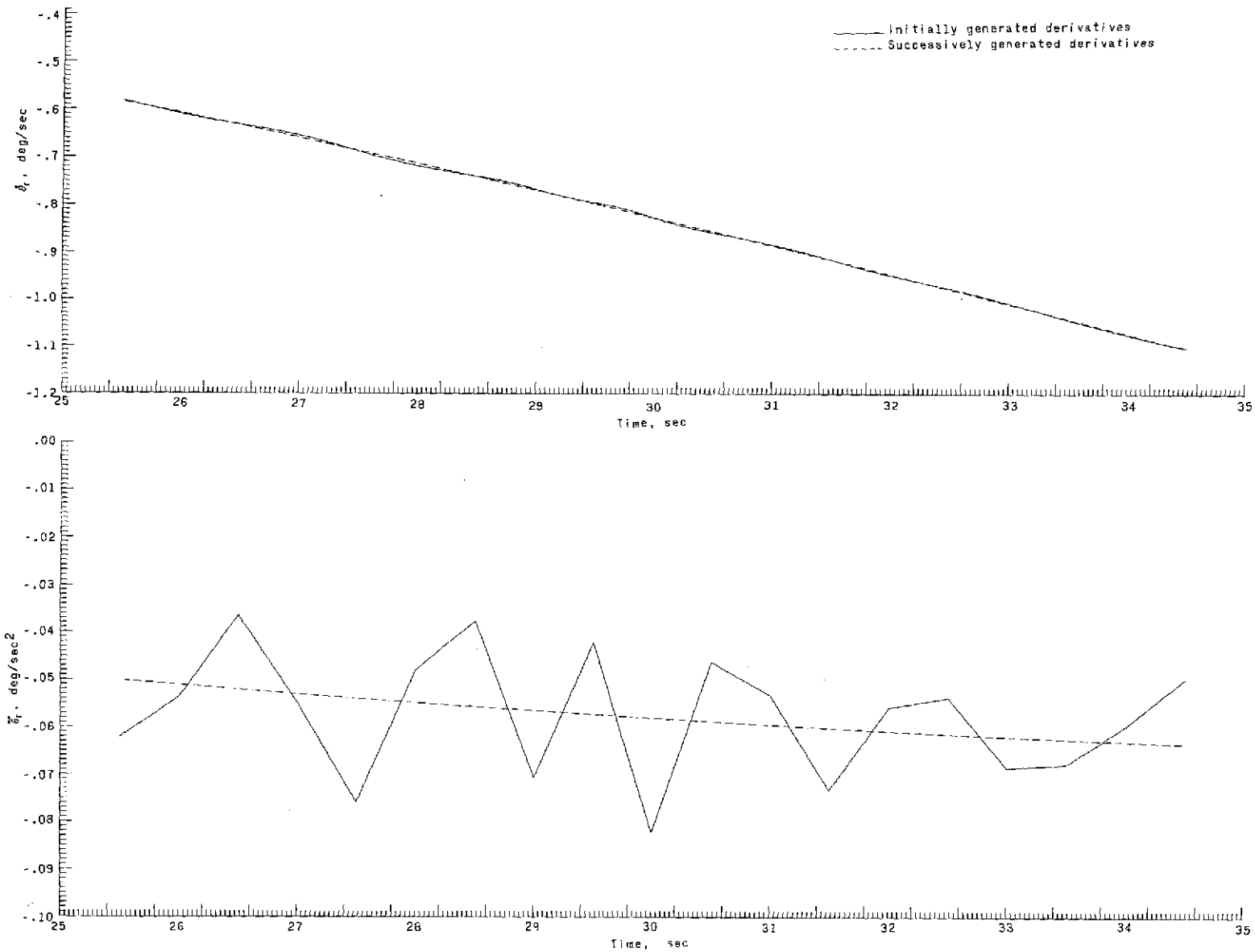

Figure 7.- Generated first and second derivatives of the elevation data.

CSA-RADFAST Method Results

A total axial-force coefficient C_X was obtained from reference 1 by algebraically adding the base and forebody axial-force coefficients presented therein. Then by noting that for small angles of attack $C_D = C_X$, the drag variation used herein for comparison purposes was realized.

The results of computing the drag coefficient versus Mach number using the previously described techniques are shown in figure 8 and are compared with the results of reference 1. It can be seen that the results of the R1 and R3 flights are inconclusive. They each have a drag rise at about the same Mach number as that of reference 1, but neither approximates the drag curve of reference 1 in appearance. On the other hand, the drag curve of R4 does approximate that of reference 1 in appearance. A small amplitude perturbation on the R4 curve, however, makes it somewhat difficult to precisely define its drag rise. It should be noted here that in this updated method no smoothing was performed on anything but the basic radar data. The resultant R4 drag curve could have been further smoothed using a priori knowledge of the wind-tunnel drag variation. Having a high level of confidence in the subsonic portion of the wind-tunnel drag variation, the perturbation in the subsonic radar drag variation would have been eliminated and the drag rise could be easily estimated. Thus, as a backup method for determining the drag rise, the radar-data-alone approach has considerable merit.

Additional Comparison

Independently of the techniques reported herein, an investigation was made by the NASA Wallops Flight Center of a Kalman Filter computer program (KAPPA) applied to radar tracking data for the purpose of estimating errors in aircraft and missile trajectories (ref. 6). One set of tracking data used in that study was, again, that of R4. In the reference, R4 is designated Supercritical Body No. 3. The only result presented therein is a plot showing a variation of drag acceleration with Earth-relative velocity. In order to be able to time correlate that result with the CSA-RADFAST results, time histories of trajectory parameters were obtained from Wallops via private communication. A comparison between the trajectory results of the two programs is shown in figure 9. It can be seen that there is very good agreement between the CSA-RADFAST and KAPPA position and velocity results. Since the model is one and the same, it was possible to vectorially add the measured winds to the Earth-relative velocity of the KAPPA program as they were in the CSA-RADFAST program, convert the drag acceleration to drag force, and attain another drag-coefficient variation. This variation is shown in figure 10 with CSA-RADFAST R4 and reference 1 drag curves. The basic shape of the KAPPA curve is similar to the others, but its drag rise occurs at a higher Mach number.

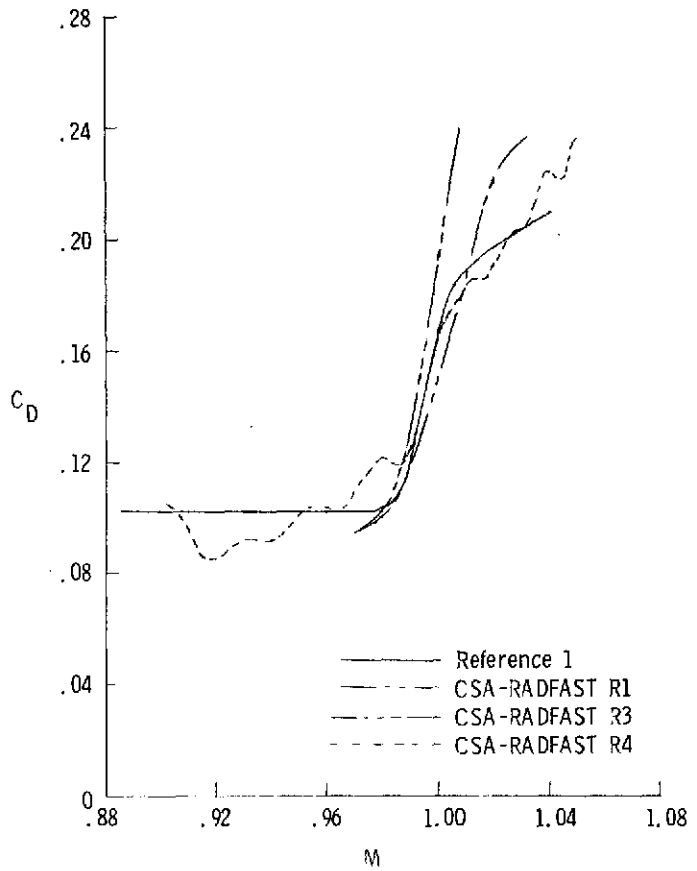

Figure 8.- Drag results obtained by the application of the CSA-RADFAST method to models of the test series compared with the results of reference 1.

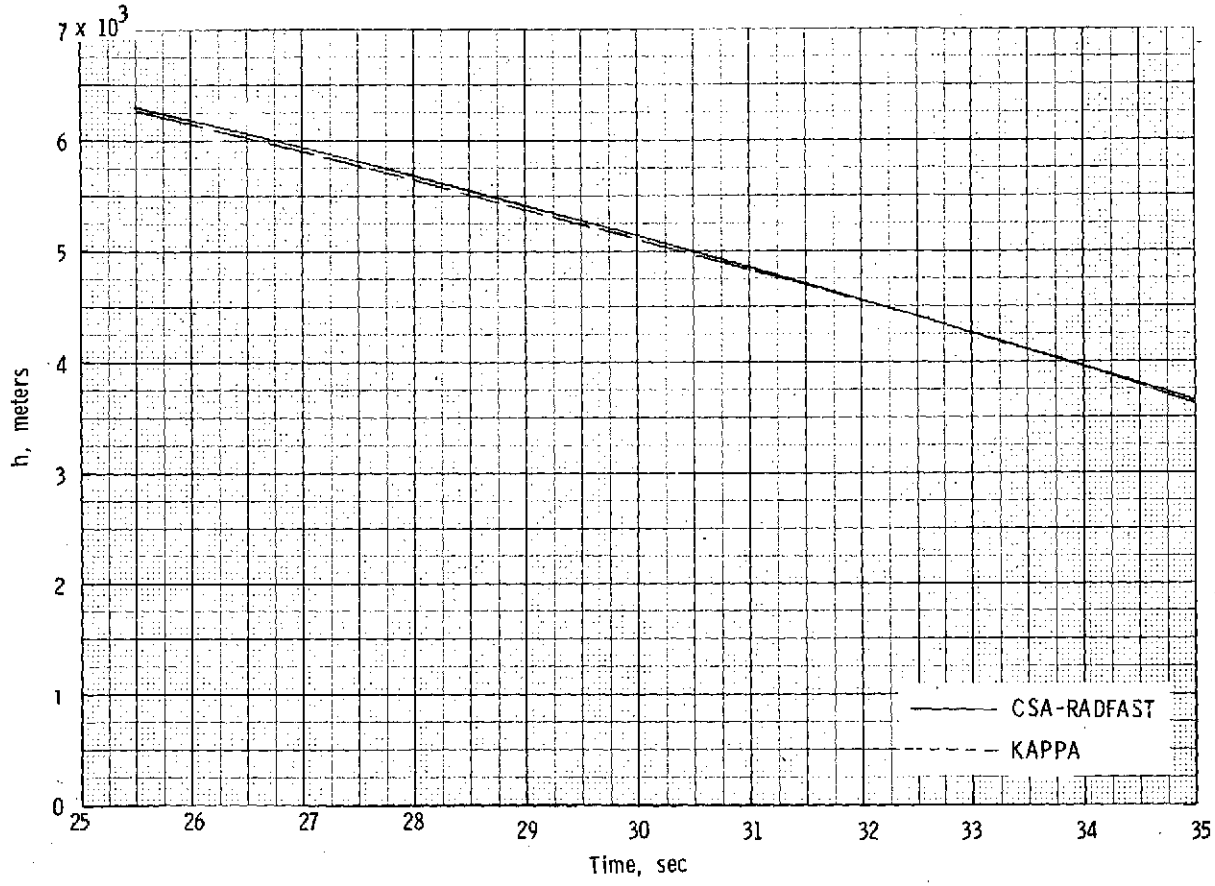

(a) Altitude.

Figure 9.- Trajectory results of the CSA-RADFAST method compared with those of the KAPPA method.

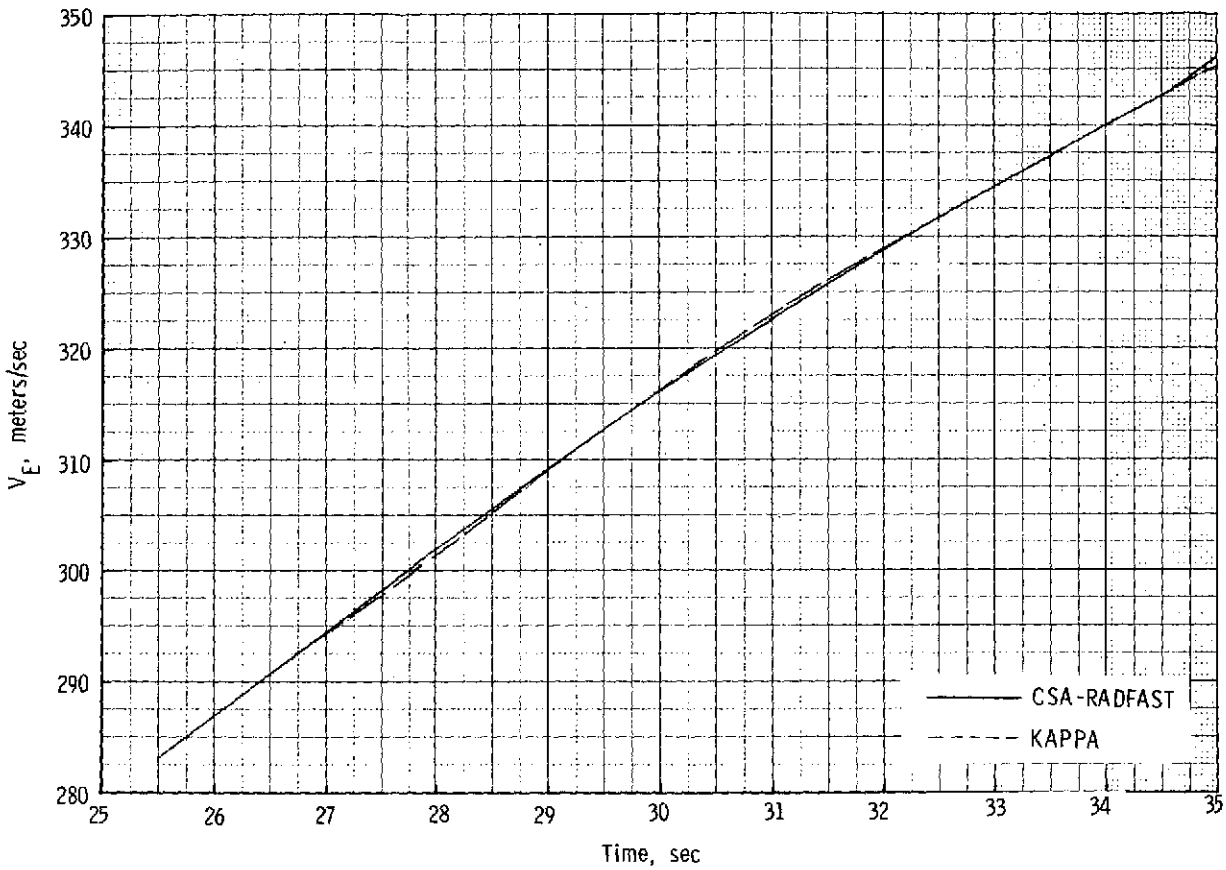

(b) Velocity.

Figure 9.- Concluded.

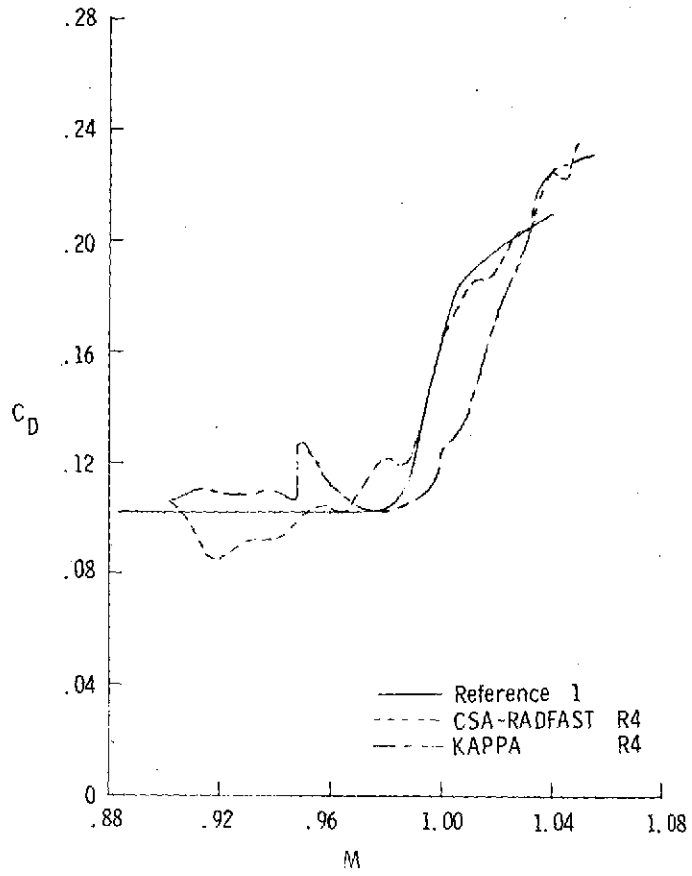

Figure 10.- R4 drag results obtained by two different radar-data-alone methods compared with the results of reference 1.

ANALYSIS OF RESULTS

In attempting to give a physical explanation for what caused the errors in CSA-RADFAST results, three possible error sources may be immediately identified: (1) the data reduction equations, (2) the smoothing techniques, and (3) the radar measurements. A six-degree-of-freedom trajectory program (ref. 5) with a radar subroutine was used to generate radar data. In addition to the four quantities $(\rho,\psi_r,\theta_r,\dot{\rho}_D)$ usually obtained from actual radar tracks, the radar subroutine also yields $\dot{\psi}_r$ and $\dot{\theta}_r$. The main program simultaneously computes the total aerodynamic force coefficient C_T, the components of which it is actually using internally in computing the trajectory. It should be remembered that for small angles of attack, $C_T \approx C_D$. The output of this generated case was designated GEN 1. In order to verify the data-reduction equations, the first derivatives $(\dot{\rho}, \dot{\psi}_r, \text{ and } \dot{\theta}_r)$ of GEN 1 were numerically differentiated to yield $\ddot{\rho}$, $\ddot{\psi}_r$, and $\ddot{\theta}_r$. These nine quantities (the three just obtained and the six from GEN 1) were then used as input to a RADFAST program modified to accept them directly. This checkout case was designated GEN 2 and its output, C_T versus M, is shown compared with the C_T versus M of GEN 1 in figure 11(a). It can be seen that there is extremely good agreement.

The next step taken to help gain an understanding of the problem was to use just the four quantities $(\rho, \psi_r, \theta_r, \text{ and } \dot{\rho}_D)$ from GEN 1 and to treat them exactly in the same manner that actual radar data (which, in fact, is comprised of only these four quantities) is treated. In accordance with the procedures described in the section entitled "Analytical Methods" these generated radar data were smoothed using the CSA/CRT technique. Its output, the coefficients to the cubic equations, were used as input to RADFAST where they were evaluated and used to compute a C_T versus M curve. This output is designated as GEN 3 and is shown compared with C_T versus M of GEN 1 in figure 11(b). It can now be seen that while some degradation has occurred the agreement between the curves is still good.

Actual radar flight data has several things which could affect the accuracy of the reduced C_D: the basic calibration of each measurement (bias, linearity, etc.), the sampling rate (Is it high enough to define all frequencies of interest?), and noise (white, black, signal-to-noise ratio, etc.). For the purpose of this study, only the effect of a fixed sampling rate and white noise with a standard deviation comparable to that found on the Wallops FPQ-6 radar is examined. First, the effect of the fixed sampling rate alone is studied and then the effect of a combination of sampling rate and noise is investigated.

The six-degree-of-freedom trajectory program has a computing interval which is controlled internally by an error-estimation criteria. In effect, the generated radar data turns out to have a variable sampling rate. However, since the variable computing

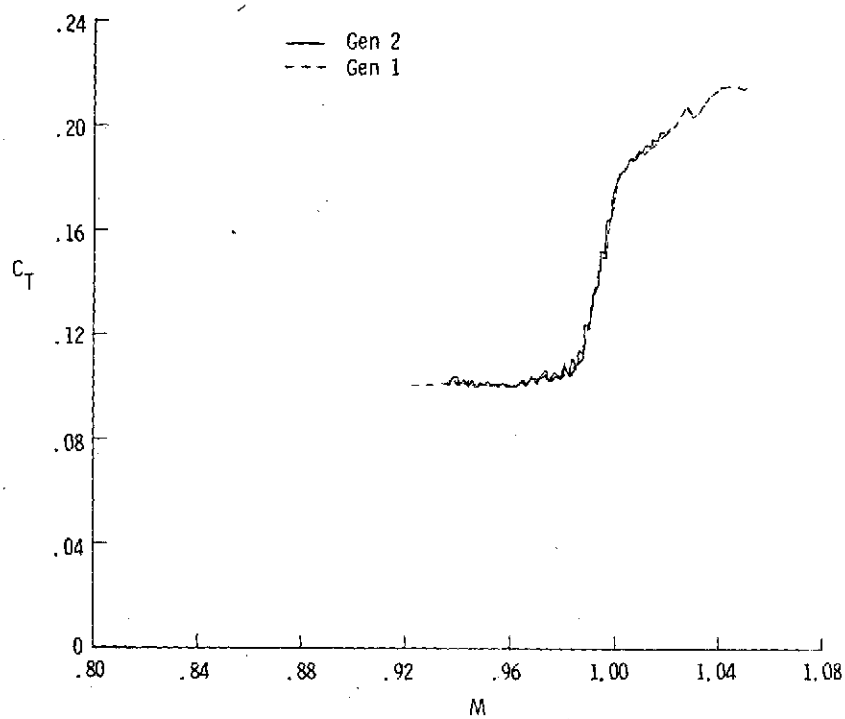

(a) Checkout case of the data reduction equations.

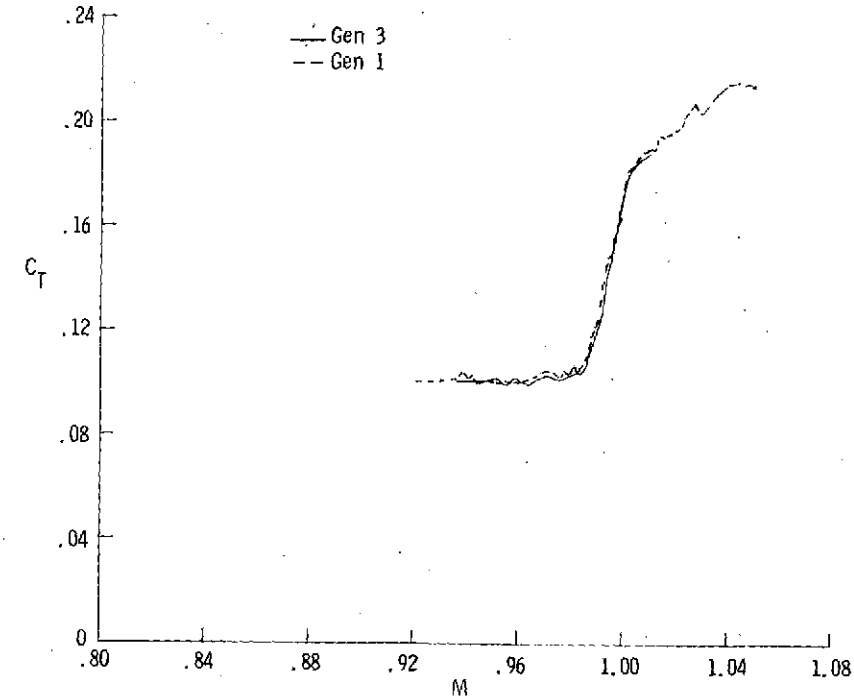

(b) Checkout case of the CSA/CRT technique.

Figure 11.- Results of a study to identify the factor most responsible for the flight results.

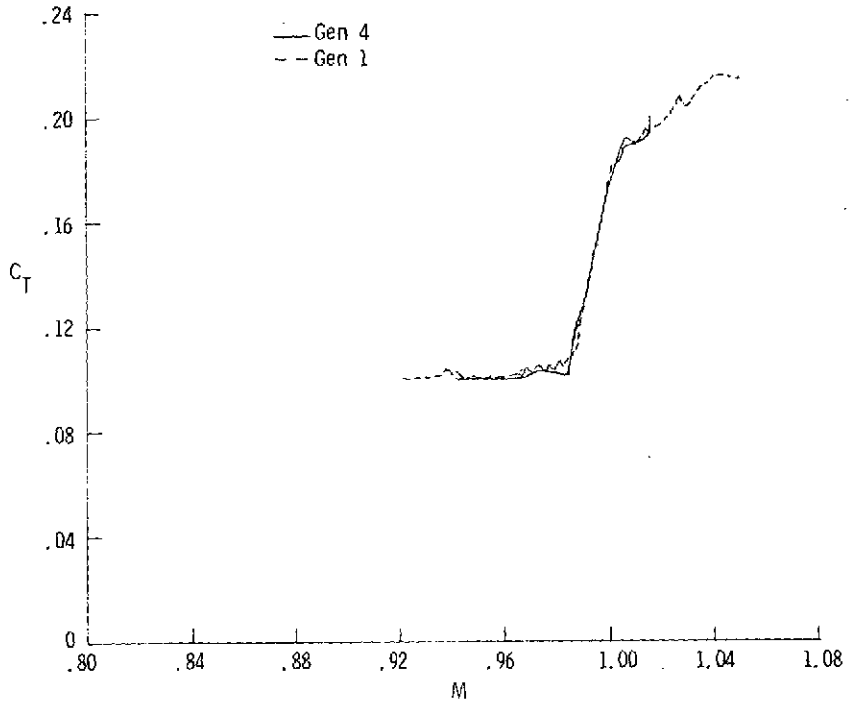

(c) Effect on the data reduction of fixed, data-sampling rate.

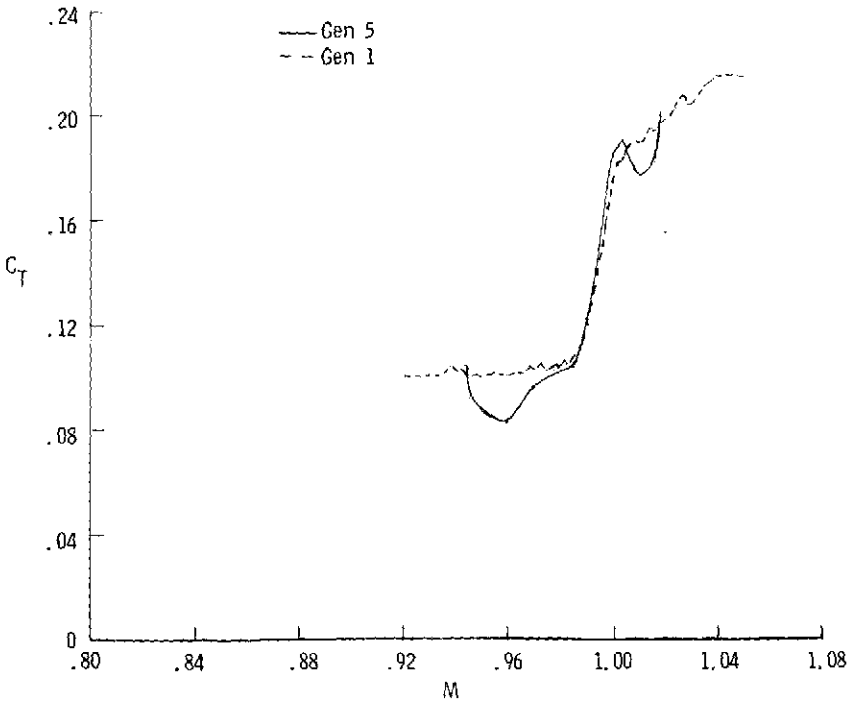

(d) Effect on the data reduction of a combination of fixed, data-sampling rate and white noise.

Figure 11.- Concluded.

(sampling) interval is generally smaller than the fixed sampled interval of the radar, it is a simple matter by interpolation to produce a new set of data with equal intervals. Again, using the procedures of the section "Analytical Methods" another C_T versus M curve, designated GEN 4, is achieved and is compared with that of GEN 1 in figure 11(c). Since the agreement is still good, it appears that a fixed data-sampling rate has a small effect on the data reduction.

White noise is random in nature, has a Gaussian (normal) distribution with a mean of zero. Quasiwhite noise was generated by a FORTRAN IV subroutine (GETRAN) with a standard deviation comparable to that found on actual radar data and algebraically added to the generated radar data of GEN 1. The following table presents the estimated standard deviation found on the Wallops FPQ-6 radar for these flights:

ρ, m	0.9144
ψ_r, deg	1.123×10^{-3}
θ_r, deg	1.123×10^{-3}
$\dot{\rho}_D$, m/sec	0.2253

By interpolation, a new set of noisy data with equal intervals was generated. And finally, once again using the data-reduction procedures, another C_T versus M curve designated GEN 5, is computed and compared with the C_T versus M curve of GEN 1 in figure 11(d). Now it is possible to see a degradation in the results comparable to that attained when using actual radar data.

Thus, in spite of employing advanced meteorological measurement techniques, optimizing the trajectory, and updating both the data reduction equations and the filtering procedures, the precise definition of the drag-rise Mach number from radar data alone is not possible because of the inadequacy of the cubic spline approximation technique to handle the noise inherently found on the Wallops tracking radars.

CONCLUDING REMARKS

An investigation was conducted of new techniques used to determine the complete transonic drag characteristics of a series of free-flight drop-test models using, for the most part, radar-tracking data only. This work was done to improve the results of that which is typically a back-up mode to the accelerometer technique used in free-flight drag studies. In this effort, exact kinematic equations tailored to enhance smoothing procedures were formulated. Preflight trajectory design optimized the contribution of the data known to be most accurate. The latest meteorological measurement systems were employed. Analytical filtering techniques supplemented by visual displays which permit

on-the-spot engineering judgment to be exercised in the postflight analysis of the data were used. The results of this exploration were compared with those obtained by a more direct, accelerometer approach using onboard, instrument data. The comparison indicated that the accelerometer drag curve was approximated by the radar-data-alone drag curve. A small amplitude perturbation on the latter curve, however, precluded a precise determination of its drag rise. On the other hand, the radar-data-alone approach has merit as a backup method, for the drag rise could be estimated. In an attempt to define physically which factor caused the above results, an analytical study using generated radar data was made. In this study it was found that the filtering techniques employed were not capable of accounting for radar noise. When the generated data were degraded by white noise comparable to that inherently found on the Wallops FPQ-6 radar, the results were essentially the same as when using real radar data.

Langley Research Center,
National Aeronautics and Space Administration,
Hampton, Va., July 11, 1974.

APPENDIX A

HAND-CALCULATION DATA-REDUCTION METHOD

The most significant equations of the method used in the past for determining the variation of drag coefficient with Mach number from principally radar data took the form:

Drag force along the flight path:

$$D = -\frac{W}{g}\left(\frac{dV_E}{dt} + g \sin \gamma_{E,p}\right) \tag{A1}$$

Earth-relative velocity:

$$V_E = \left\{\rho^2\left[\dot{\theta}_r^2 + \left(\dot{\psi}_r \cos \theta_r\right)^2\right] + \dot{\rho}_D^2\right\}^{1/2} \tag{A2}$$

Free-stream velocity:

$$V_\infty = V_E + V_W \cos\left(\gamma_{E,y} - \psi_W\right)\cos \gamma_{E,p} \tag{A3}$$

Drag coefficient:

$$C_D = \frac{D}{q_\infty S} \tag{A4}$$

These equations were formulated based on the following assumptions:

(1) Ballistic flight vehicles would fly at small angles of attack and consequently all aerodynamic force would be drag force.

(2) Other than the drag force, the only force acting along the flight path would be a component of the model weight. The acceleration proportional to the algebraic sum of the above forces is the scalar magnitude of the velocity-vector rate of change.

(3) The Earth is considered flat and nonrotating due to the close proximity of the flight vehicle to the radar and the shortness of flight duration.

The first assumption is of utmost importance and is examined in some detail in appendix C. The second assumption forms the basis for equation (A1) which sums the forces along the radar flight path (the Earth-relative velocity vector). Drag acts along the free-stream velocity vector; however, at the test speeds of interest and the low actual wind velocities, these two velocity vectors are almost coincident. The first part of the third assumption is quite appropriate. The Earth could be considered flat for flights of interest here. The second part of the third assumption, however, is erroneous. While

the duration of the flights was short (on the order of 10 sec for the helium-gun flight tests), the Coriolis forces which arise from tracking a free-flight body using a fixed radar on a rotating Earth act on the flight model the entire time, no matter how short, and consequently influence the force coefficients which are being sought. For low drag models the Coriolis forces can be significant. In the original helium-gun test setup (see fig. A1) the models were launched directly away from the Doppler radar set and usually into or with the surface winds. The models were launched with low elevation angles and quite often reached an altitude no greater than 610 m. In many cases the models were flying more or less horizontally in the region of interest. Thus, the free-stream velocity could, for the most part, be obtained merely by adding or subtracting, depending on its direction, the actual wind speed. In equation form,

$$V_\infty = V_E \pm V_W \tag{A5}$$

The sign would be positive for a headwind and negative for a tailwind. Since the line of sight from the Doppler radar set was, for all practical purposes, tangent to the model flight path throughout the test region, it was also possible to consider the Earth-relative velocity to be composed entirely of the velocity obtained from the Doppler set $\left(V_E = \dot{\rho}_D\right)$. Furthermore, the rate of change of this Doppler velocity was the dV_E/dt used in equation (A1). In some of the helium-gun flights and many of the rocket-propelled flights, these special flight conditions were not possible and more complete expressions had to be employed. The velocity equation was modified to include the transverse components of motion as well as the radial one (see eq. (A2)). Correction factors were applied to equation (A5) to account for wind which were other than headwinds or tailwinds and for the cases where models were not flying horizontally (see eq. (A3)). The second assumption, however, where only quantities acting along the flight path are considered, was maintained so that equation (A5) was modified only in such a manner as to consider the component of the actual wind parallel to the flight path. An even more complete expression would have been to vectorially add the winds to the Earth-relative velocity.

The free use of equation (A5) has been responsible for the erroneous practice by some analysts of using the time-differentiated free-stream velocity dV_∞/dt in equation (A1). This error is not immediately detectable because with a constant wind velocity and a near constant flight altitude, dV_∞/dt is equal to dV_E/dt. However, while the wind may be constant at a given altitude, it does usually change with altitude. If the flight vehicle is changing altitude and if the time-differentiated free-stream velocity is used, an acceleration is introduced which is equal to the product of dV_W/dh and dh/dt, where the former is the change in wind velocity with altitude and the latter is the change in altitude of the flight vehicle with time. This can be shown in equation form by differentiating equation (A5) as

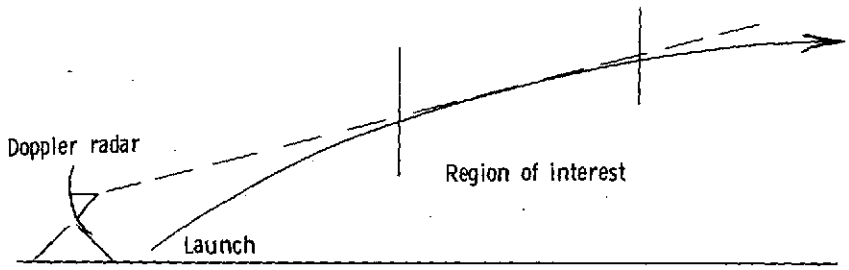

(a) View of vertical line-of-sight plane of Doppler radar.

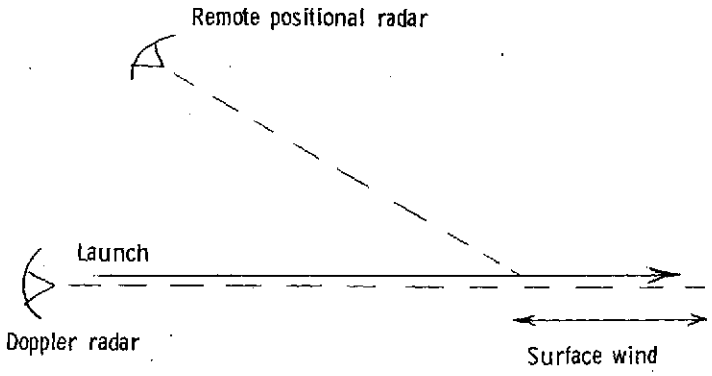

(b) Overhead view.

Figure A1.- Schematic of the launch model typically used in the past.

$$\frac{dV_\infty}{dt} = \frac{dV_E}{dt} \pm \frac{dV_w}{dt}$$

where it can be seen that

$$\frac{dV_w}{dt} = \frac{dV_w}{dh}\frac{dh}{dt}$$

Obviously, in the flight-test cases of constant altitude the dV_w/dt term vanishes. For the other cases dV_w/dt does exist but is an acceleration that has nothing to do with the external forces acting on the flight vehicle.

Management and Reduction of Data to Coefficient Form

The hand-calculation method was aimed directly toward determining the variation of drag with Mach number. For instance, it computes only enough trajectory parameters to correlate the meteorological quantities with the aerodynamic forces. The method is presented in a step-by-step manner as follows:

(1) Plot the raw radar data $\left(\rho,\psi_r,\theta_r,\dot{\rho}_D\right)$ versus time (t), hand fair the plots, and read smooth values of same

(2) Compute altitude (h), horizontal range (R), north-south component of horizontal range (x), and the east-west component of horizontal range (y) using smooth values of ρ, ψ_r, and θ_r

$$h = \rho \sin \theta_r \tag{A6}$$

$$R = \rho \cos \theta_r \tag{A7}$$

$$x = R \cos \psi_r \tag{A8}$$

$$y = R \sin \psi_r \tag{A9}$$

(3) Plot h versus R, hand fair the plot, and read slopes from the faired plot to obtain the flight-path angle in the vertical plane $\left(\gamma_{E,p}\right)$

$$\gamma_{E,p} = \tan^{-1}\frac{\Delta h}{\Delta R} \tag{A10}$$

(4) Plot x versus y, hand fair the plot, and read slopes from the faired plot to obtain the flight-path angle in the horizontal plane $\left(\gamma_{E,y}\right)$

$$\gamma_{E,y} = \tan^{-1} \frac{\Delta y}{\Delta x} \tag{A11}$$

(5) Plot smooth values of ψ_r and θ_r versus t, read slopes from the respective plots to obtain $\dot{\psi}_r$ and $\dot{\theta}_r$

$$\left.\begin{aligned} \dot{\psi}_r &= \frac{\Delta \psi_r}{\Delta t} \\ \dot{\theta}_r &= \frac{\Delta \theta_r}{\Delta t} \end{aligned}\right\} \tag{A12}$$

(6) Plot $\dot{\psi}_r$ and $\dot{\theta}_r$ versus t, hand fair the plots, read smooth values of $\dot{\psi}_r$ and $\dot{\theta}_r$, and convert the units of these quantities from deg/sec to rad/sec

(7) Compute the Earth-relative velocity with respect to the radar $\left(V_E\right)$ using equation (A2) and the above converted $\dot{\psi}_r$ and $\dot{\theta}_r$

(8) Plot V_E versus t, hand fair the plot, and read slopes off the plot to obtain the scalar magnitude of the velocity-vector rate of change $\left(dV_E/dt\right)$

(9) Plot dV_E/dt versus t, hand fair the plot, read smooth values of dV_E/dt, and compute the drag (D) using equation (A1)

(10) Using wind speed $\left(V_w\right)$ and wind direction $\left(\psi_w\right)$ from the radiosonde data, compute free-stream velocity $\left(V_\infty\right)$ using equation (A3)

(11) Using density $\left(\rho_\infty\right)$ and speed of sound $\left(V_c\right)$ from the radiosonde data, compute dynamic pressure $\left(q_\infty\right)$ and Mach number (M)

$$q_\infty = \frac{1}{2} \rho_\infty V_\infty^2 \tag{A13}$$

$$M = \frac{V_\infty}{V_c} \tag{A14}$$

(12) Finally, compute drag coefficient $\left(C_D\right)$ using equation (A4).

APPENDIX B

EQUATIONS OF THE NEW DATA-REDUCTION METHOD (RADFAST)

This appendix presents the equations used herein to determine the kinematic motions of a vehicle in free flight over a rotating oblate spheroid and the variation of drag coefficient with Mach number (RADFAST). These equations were formulated in such a manner that each radar measurement and its applicable derivatives could be used directly in the determination of the flight trajectory and the drag-coefficient variation with Mach number. The purpose of this approach was to enable any one set of data to be smoothed independently of any other set. Thus, after the contribution of a particularly accurate set of data as a component of a total desired quantity had been maximized by preflight trajectory design, it would not then be degraded by being mixed with much less accurate data and then smoothed. This approach also facilitates the introduction of the Doppler velocity $\dot{\rho}_D$ in the data reduction procedure.

In addition to updating the techniques for obtaining drag coefficients from radar data alone, this program also updates the trajectory program and is compatible with the six-degree-of-freedom trajectory program of reference 2 which is widely used by NASA Langley Research Center, NASA Wallops Flight Center, and others.

The equations are written in a straightforward manner and are presented in an outline format as follows:

I. Determination of the constants associated with the tracking radar station (fig. B1(a)).

A. Geocentric latitude of the sea-level subradar point $\phi_C\left(OR_{SL}\right)$ is determined by

$$\phi_C\left(OR_{SL}\right) = \tan^{-1}\left[\frac{b^2}{a^2}\tan\phi_G\left(OR_{SL}\right)\right] \tag{B1}$$

where the geodetic latitude of the radar, $\phi_G\left(OR_{SL}\right) \equiv \phi_G(OR)$, and the polar and equatorial radii of the earth b and a, respectively, are known.

B. The geocentric radius vector of the sea-level subradar point $R_C\left(OR_{SL}\right)$ is found by

$$R_C\left(OR_{SL}\right) = \frac{ab}{\sqrt{b^2\cos^2\phi_C\left(OR_{SL}\right) + a^2\sin^2\phi_C\left(OR_{SL}\right)}} \tag{B2}$$

C. The geodetic radius vector of the sea-level subradar point $R_G\left(OR_{SL}\right)$ is given by

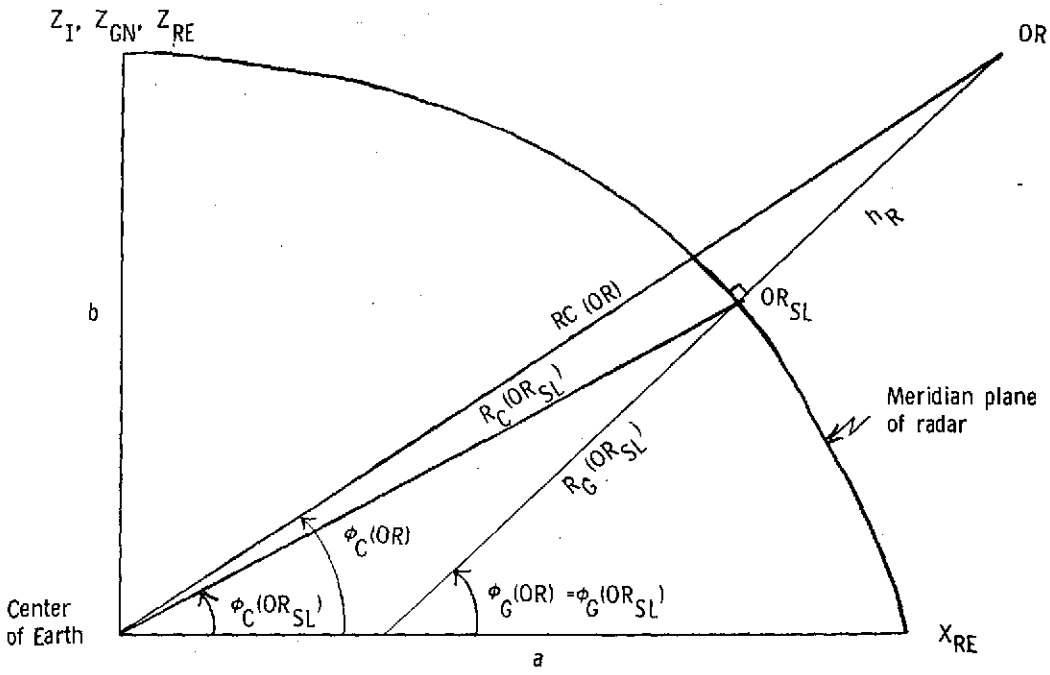

(a) Meridian plane view showing detailed geocentric and geodetic latitude relationships of the radar station OR.

Figure B1.- Radar-station relationships with respect to Earth.

$$R_G\left(OR_{SL}\right) = R_C\left(OR_{SL}\right) \frac{\sin \phi_C\left(OR_{SL}\right)}{\sin \phi_G\left(OR_{SL}\right)} \tag{B3}$$

D. The geodetic radius vector of the radar itself $R_G(OR)$ is found merely by adding the height of the radar above sea level h_R as follows:

$$R_G(OR) = R_G\left(OR_{SL}\right) + h_R \tag{B4}$$

E. The geocentric radius vector of the radar itself $R_C(OR)$ is determined by

$$R_C(OR) = \sqrt{R_C\left(OR_{SL}\right)^2 + h_R^2 + 2\left[R_C\left(OR_{SL}\right)\right]\left[h_R\right]\cos \sigma} \tag{B5}$$

where

$$\sigma = \phi_G\left(OR_{SL}\right) - \phi_C\left(OR_{SL}\right)$$

F. Finally, the geocentric latitude of the radar itself $\phi_C(OR)$ is calculated by

$$\phi_C(OR) = \sin^{-1}\left[\frac{R_G(OR)}{R_C(OR)} \sin \phi_G(OR)\right] \tag{B6}$$

II. Determination of the positional displacement of the flight vehicle with respect to various axis systems (figs. B1(b) and B1(c)).

A. The position of the flight-vehicle origin relative to the geodetic axis system of the radar $X_{OR}(O)_G$ is determined by

$$X_{OR}(O)_G = \begin{bmatrix} \rho \cos \theta_r \cos \psi_r \\ \rho \cos \theta_r \sin \psi_r \\ -\rho \sin \theta_r \end{bmatrix} \tag{B7}$$

The X_{OR}-axis is directed toward the North Pole and the Z_{OR}-axis is directed downward. The symbols x_{OR}, y_{OR}, and z_{OR} are components of $X_{OR}(O)_G$.

B. The position of the flight-vehicle origin relative to a rotating, Earth-centered, radar axis system $X_{RE}(O)_E$ is calculated by

$$X_{RE}(O)_E = \left[T_1\right] X_{OR}(O)_G + \begin{bmatrix} R_C(OR)\cos \phi_C(OR) \\ 0 \\ R_C(OR)\sin \phi_C(OR) \end{bmatrix} \tag{B8}$$

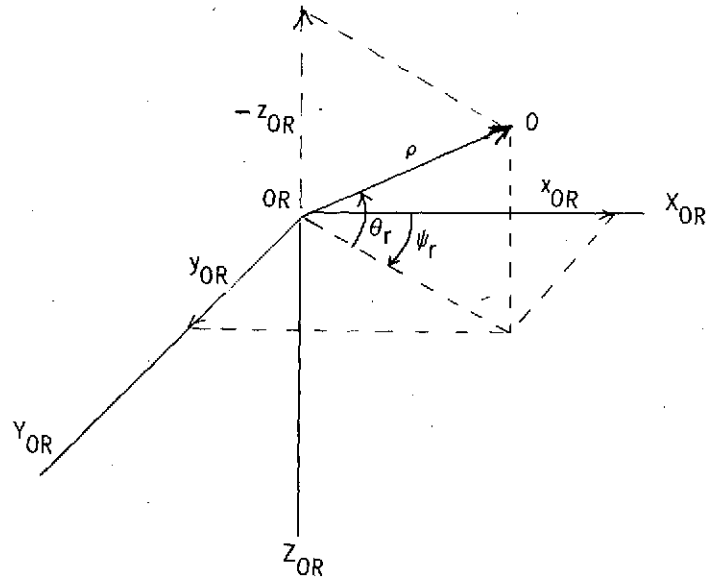

(b) Positional displacement of the flight vehicle O with respect to the geodetic axis system of the radar station OR.

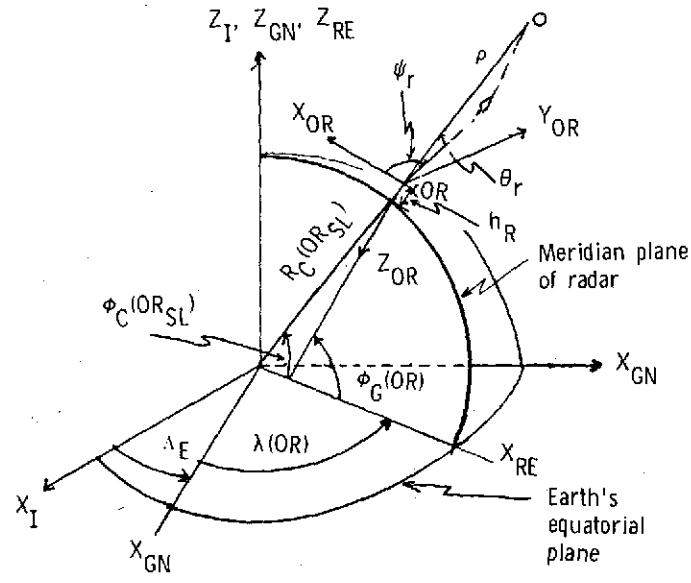

(c) Overall view showing the relationship of the radar axis system to the Earth-centered axis systems.

Figure B1.- Concluded.

where $[T_1]$ is a simple, time-invariant transformation matrix defined in equation (B48). The X_{RE}-axis lies in the equatorial plane and passes through the meridian of the radar. The Z_{RE}-axis passes through the North Pole. The symbols x_{RE}, y_{RE}, and z_{RE} are components of $X_{RE}(O)_E$.

C. The position of the flight-vehicle origin relative to a rotating, Earth-centered, Greenwich axis system $X_{GN}(O)_E$ is found by

$$X_{GN}(O)_E = [T_2]X_{RE}(O)_E \tag{B9}$$

where $[T_2]$ is another simple, time-invariant transformation matrix in equation (B49). The X_{GN}-axis lies in the equatorial plane and passes through the meridian of Greenwich, England. The Z_{GN}-axis passes through the North Pole. The symbols x_{GN}, y_{GN}, and z_{GN} are components of $X_{GN}(O)_E$.

D. Finally, the position of the flight-vehicle origin relative to a nonrotating, Earth-centered, inertial axis system $X_I(O)_I$ is determined by

$$X_I(O)_I = [T_3(t)]X_{GN}(O)_E \tag{B10}$$

where $[T_3(t)]$ is a time-dependent transformation matrix defined in equation (B50). The Z_I-axis also passes through the North Pole. The X_I-axis lies in the equatorial plane and is related to X_E by a phase angle Λ_E. The symbols x_I, y_I, and z_I are components of $X_I(O)_I$.

Finally, Λ_E is determined by

$$\Lambda_E = \Lambda_{E,O} + \omega_E(t - t_O) \tag{B11}$$

where ω_E is the Earth's angular velocity and t is time.

III. Determination of the velocity of the flight vehicle with respect to various axis systems.

A. Velocity of the flight-vehicle origin relative to the $X_{OR}(O)_G$-axis system can be determined by

$$V_{OR}(O)_G = \dot{X}_{OR}(O)_G = [M(t)]\begin{bmatrix}\dot{\psi}_r\\ \dot{\theta}_r\\ \dot{\rho}_D\end{bmatrix} \tag{B12}$$

where $[M(t)]$ is a time-dependent matrix defined in equation (B51). The Doppler velocity $\dot{\rho}_D$ is introduced at this point.

B. Velocity of the flight-vehicle origin relative to the $X_{RE}(O)_E$-axis system is

$$V_{RE}(O)_E = \dot{X}_{RE}(O)_E = \left[T_1\right]\dot{X}_{OR}(O)_G \tag{B13}$$

C. Velocity of the flight-vehicle origin relative to the $X_{GN}(O)_E$-axis system is

$$V_{GN}(O)_E = \dot{X}_{GN}(O)_E = \left[T_2\right]\dot{X}_{RE}(O)_E \tag{B14}$$

D. Velocity of the flight-vehicle origin relative to the $X_I(O)_I$-axis system is

$$V_I(O)_I = \dot{X}_I(O)_I = \left[\dot{T}_3(t)\right]X_{GN}(O)_E + \left[T_3(t)\right]\dot{X}_{GN}(O)_E \tag{B15}$$

Note that $V_I(O)_I$ is generally referred to as the inertial velocity of the body with respect to the inertial axis system.

IV. Determination of the acceleration of the flight vehicle with respect to various axis systems.

A. Acceleration of the flight-vehicle origin relative to the $X_{OR}(O)_G$-axis system is

$$A_{OR}(O)_G = \dot{V}_{OR}(O)_G = \ddot{X}_{OR}(O)_G = \left[\dot{M}(t)\right]\begin{bmatrix}\dot{\psi}_r\\ \dot{\theta}_r\\ \dot{\rho}_D\end{bmatrix} + \left[M(t)\right]\begin{bmatrix}\ddot{\psi}_r\\ \ddot{\theta}_r\\ \ddot{\rho}_D\end{bmatrix} \tag{B16}$$

B. Acceleration of the flight-vehicle origin relative to the $X_{RE}(O)_E$-axis system is

$$A_{RE}(O)_E = \dot{V}_{RE}(O)_E = \ddot{X}_{RE}(O)_E = \left[T_1\right]\ddot{X}_{OR}(O)_G \tag{B17}$$

C. Acceleration of the flight-vehicle origin relative to the $X_{GN}(O)_E$-axis system is

$$A_{GN}(O)_E = \dot{V}_{GN}(O)_E = \ddot{X}_{GN}(O)_E = \left[T_2\right]\ddot{X}_{RE}(O)_E \tag{B18}$$

D. Acceleration of the flight vehicle origin relative to the $X_I(O)_I$-axis system is

$$A_I(O)_I = \dot{V}_I(O)_I = \ddot{X}_I(O)_I = \left[\ddot{T}_3(t)\right]X_{GN}(O)_E + 2\left[\dot{T}_3(t)\right]\dot{X}_{GN}(O)_E + \left[T_3(t)\right]\ddot{X}_{GN}(O)_E \tag{B19}$$

V. Determination of the flight-trajectory positions and orientations (fig. B2).

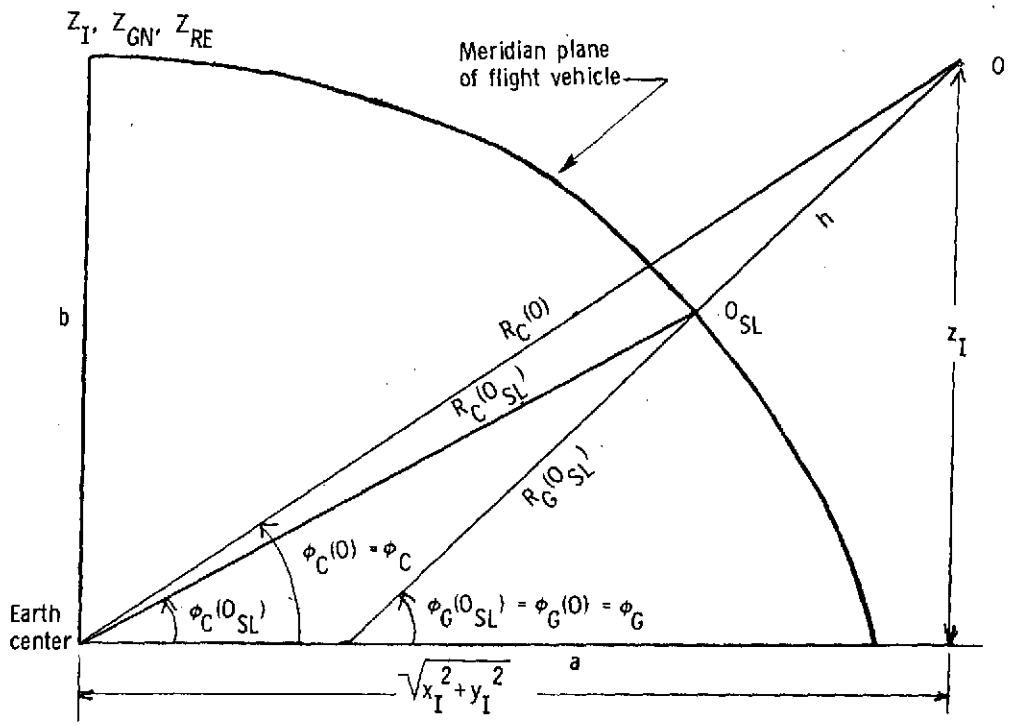

(a) Meridian plane view showing detailed geocentric and geodetic latitude relationships of the flight vehicle O.

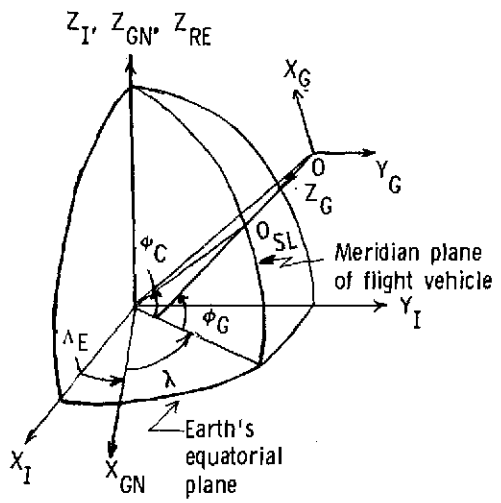

(b) Overall view showing the relationship of the flight-vehicle axis system to the Earth-centered axis systems.

Figure B2.- Flight-vehicle relationships with respect to Earth.

A. Geocentric latitude of the flight vehicle, ϕ_C, is

$$\phi_C = \tan^{-1}\left(\frac{z_I}{\sqrt{x_I^2 + y_I^2}}\right) \tag{B20}$$

where x_I, y_I, and z_I are components of $X_I(O)_I$.

B. Longitude of the flight vehicle, $\lambda_C = \lambda_G = \lambda$, is

$$\lambda = \tan^{-1}\left(\frac{y_I}{x_I}\right) - \Lambda_E \tag{B21}$$

C. Geocentric radius vector of the flight vehicle, $R_C(O)$, is

$$R_C(O) = \sqrt{x_I^2 + y_I^2 + z_I^2} \tag{B22}$$

D. Geodetic latitude of the flight vehicle, ϕ_G, is

$$\phi_G = \tan^{-1}\left[\mu_3\left(\frac{a}{b}\right)\frac{\sin\phi_C}{\cos\phi_C}\right] \tag{B23}$$

where μ_3 is an auxiliary function computed by starting with $\mu_0 = 1$ and iterating until μ_3 is determined by the expression

$$\mu_n = \frac{b}{a} + \frac{\frac{a^2 - b^2}{a}(\mu_{n-1})}{R_C(O)\sqrt{\cos^2\phi_C + (\mu_{n-1})^2\sin^2\phi_C}} \tag{B24}$$

E. Geocentric latitude of the sea level, subflight vehicle point, $\phi_C(O_{SL})$, is

$$\phi_C(O_{SL}) = \tan^{-1}\left(\frac{b^2}{a^2}\tan\phi_G\right) \tag{B25}$$

F. Geocentric radius vector of the sea level, subflight vehicle point, $R_C(O_{SL})$, is

$$R_C(O_{SL}) = \frac{ab}{\sqrt{b^2\cos^2\phi_C(O_{SL}) + a^2\sin^2\phi_C(O_{SL})}} \tag{B26}$$

G. Geodetic radius vector of the sea level, subflight vehicle point, $R_G(O_{SL})$, is

$$R_G(O_{SL}) = R_C(O_{SL})\frac{\sin\phi_C(O_{SL})}{\sin\phi_G} \tag{B27}$$

H. Finally, the altitude above sea level h is determined by

$$h = \frac{z_I}{\sin \phi_G} - R_G\left(O_{SL}\right) \tag{B28}$$

when $\sin \phi_G \neq 0$ and by

$$h = R_C(O) - a \tag{B29}$$

when $\sin \phi_G = 0$.

The geodetic axis system of the flight vehicle $X(O)_G$ may now be defined. The X_G-axis is directed north, the Y_G-axis is directed east, and the Z_G-axis is directed down along the geodetic radius vector of the flight vehicle.

VI. Determination of flight-trajectory velocities (fig. B3).

A. Inertial velocity of the flight vehicle with respect to its geodetic axis system is

$$V_I(O)_G = \left[\tilde{T}_{G2I}\right] V_I(O)_I \tag{B30}$$

where $\left[\tilde{T}_{G2I}\right]$ is a time-dependent transformation matrix defined in equation (B52).

B. Velocity relative to the Earth of the flight vehicle with respect to its geodetic axis system is

$$V_E(O)_G = V_I(O)_G - \left\{\omega_E \begin{bmatrix} 0 \\ R_C(O) \\ 0 \end{bmatrix} \cos \phi_C\right\} \tag{B31}$$

The magnitude of Earth-relative velocity V_E is

$$V_E = \left| V_E(O)_G \right| \tag{B32}$$

The flight-path angles associated with this velocity are

$$\gamma_{E,p} = \tan^{-1}\left[\frac{-V_E(O)_{kG}}{\sqrt{V_E(O)_{iG}^2 + V_E(O)_{jG}^2}}\right] \tag{B33}$$

in the vertical plane and

$$\gamma_{E,y} = \tan^{-1}\left[\frac{V_E(O)_{jG}}{V_E(O)_{iG}}\right] \tag{B34}$$

in the horizontal plane.

C. Velocity relative to the free stream of the flight vehicle with respect to its geodetic axis system is

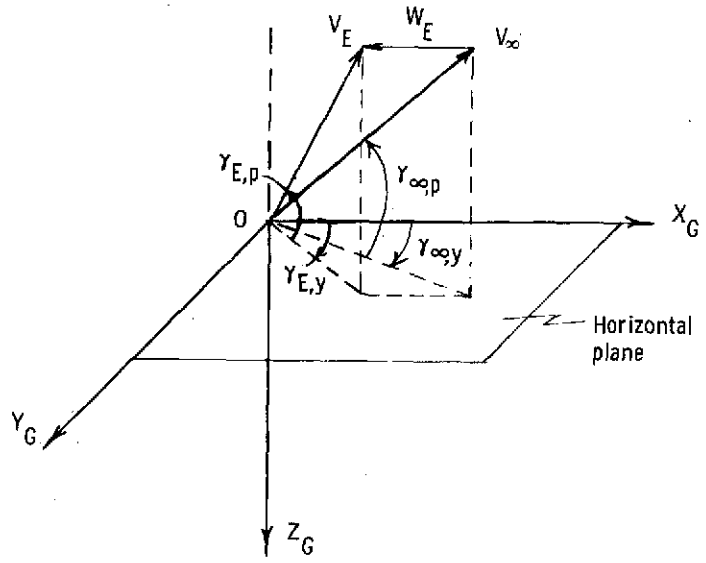

Figure B3.- Earth-relative and free-stream velocity vector orientation of the flight vehicle with respect to its geodetic axis system.

$$V_\infty(O)_G = V_E(O)_G - W_E(O)_G \tag{B35}$$

where $W_E(O)_G$ is the wind velocity relative to Earth with respect to the geodetic axis system of the flight vehicle and where W_E is the magnitude of $W_E(O)_G$.

The magnitude of the free-stream velocity V_∞ is

$$V_\infty = \left| V_\infty(O)_G \right| \tag{B36}$$

The flight-path angles associated with this velocity are

$$\gamma_{\infty,p} = \tan^{-1}\left[\frac{-V_\infty(O)_{kG}}{\sqrt{V_\infty(O)_{iG}^2 + V_\infty(O)_{jG}^2}}\right] \tag{B37}$$

in the vertical plane and

$$\gamma_{\infty,y} = \tan^{-1}\left[\frac{V_\infty(O)_{jG}}{V_\infty(O)_{iG}}\right] \tag{B38}$$

in the horizontal plane.

VII. Gravitational acceleration at the flight-vehicle origin given in various axis systems.

A. The gravitational acceleration at the flight-vehicle origin in the geocentric axis system of the flight vehicle is defined as

$$G_I(O)_C = \begin{bmatrix} -G_T \\ O \\ G_R \end{bmatrix} \tag{B39}$$

where

$$G_T = \left\{A_1\left[\frac{a}{R_C(O)}\right]^4 - 2A_2\left[\frac{a}{R_C(O)}\right]^6\left[7\sin^2\phi_C - 3\right]\right\}\sin 2\phi_C \tag{B40}$$

and

$$G_R = A_O\left[\frac{a}{R_C(O)}\right]^2 - A_1\left[\frac{a}{R_C(O)}\right]^4\left[3\sin^2\phi_C - 1\right] + A_2\left[\frac{a}{R_C(O)}\right]^6\left(35\sin^4\phi_C - 30\sin^2\phi_C + 3\right) \tag{B41}$$

and A_0, A_1, A_2 are oblate Earth gravity constants and

$$A_0 = 9.798141 \text{ m/sec}^2$$

$$A_1 = 0.016050 \text{ m/sec}^2$$

$$A_2 = 0.0000148 \text{ m/sec}^2$$

B. The gravitational acceleration at the flight-vehicle origin in the inertial axis system is

$$G_I(O)_I = \left[T_{C2I}\right] G_I(O)_C \tag{B42}$$

where $\left[T_{C2I}\right]$ is a time-dependent transformation matrix defined in equation (B53).

VIII. Determination of drag coefficient C_D versus Mach number M.

A. The total aerodynamic force $F_I^A(O)_I$ is calculated using Newton's law as follows:

$$F_I^A(O)_I = m\left[A_I(O)_I - G_I(O)_I\right] \tag{B43}$$

where m is the mass of the flight vehicle.

B. Introducing measured values of free-stream density ρ_∞ and free-stream speed of sound V_c, the total aerodynamic force coefficient C_T is

$$C_T = \frac{\left|F_I^A(O)_I\right|}{q_\infty S} \tag{B44}$$

where S is the reference area and the dynamic pressure q_∞ is

$$q_\infty = \frac{1}{2}\rho_\infty V_\infty^2 \tag{B45}$$

and Mach number M is

$$M = \frac{V_\infty}{V_c} \tag{B46}$$

C. Finally, assuming very small angles of attack during the data period ($\eta \approx 0$),

$$C_D \approx C_T \tag{B47}$$

IX. Matrices.

$$\left[T_1\right] = \begin{bmatrix} -\sin \phi_G(OR) & 0 & -\cos \phi_G(OR) \\ 0 & 1 & 0 \\ \cos \phi_G(OR) & 0 & -\sin \phi_G(OR) \end{bmatrix} \tag{B48}$$

$$\left[T_2\right] = \begin{bmatrix} \cos \lambda_R & -\sin \lambda_R & 0 \\ \sin \lambda_R & \cos \lambda_R & 0 \\ 0 & 0 & 1 \end{bmatrix} \tag{B49}$$

$$\left[T_3(t)\right] = \begin{bmatrix} \cos \Lambda_E & -\sin \Lambda_E & 0 \\ \sin \Lambda_E & \cos \Lambda_E & 0 \\ 0 & 0 & 1 \end{bmatrix} \tag{B50}$$

$$\left[M(t)\right] = \begin{bmatrix} -y_{OR} & \dfrac{x_{OR}z_{OR}}{\sqrt{x_{OR}^2 + y_{OR}^2}} & \dfrac{x_{OR}}{\rho} \\ x_{OR} & \dfrac{y_{OR}z_{OR}}{\sqrt{x_{OR}^2 + y_{OR}^2}} & \dfrac{y_{OR}}{\rho} \\ 0 & -\sqrt{x_{OR}^2 + y_{OR}^2} & \dfrac{z_{OR}}{\rho} \end{bmatrix} \tag{B51}$$

where x_{OR}, y_{OR}, z_{OR} are components of $X_{OR}(O)_G$ and $\rho = \sqrt{x_{OR}^2 + y_{OR}^2 + z_{OR}^2}$.

$$\left[T_{G2I}\right] = \begin{bmatrix} -\sin \phi_G \cos\left(\Lambda_E + \lambda\right) & -\sin\left(\Lambda_E + \lambda\right) & -\cos \phi_G \cos\left(\Lambda_E + \lambda\right) \\ -\sin \phi_G \sin\left(\Lambda_E + \lambda\right) & \cos\left(\Lambda_E + \lambda\right) & -\cos \phi_G \sin\left(\Lambda_E + \lambda\right) \\ \cos \phi_G & 0 & -\sin \phi_G \end{bmatrix} \tag{B52}$$

Similarly,

$$\left[T_{C2I}\right] = \begin{bmatrix} -\sin\phi_C \cos\left(\Lambda_E + \lambda\right) & -\sin\left(\Lambda_E + \lambda\right) & -\cos\phi_C \cos\left(\Lambda_E + \lambda\right) \\ -\sin\phi_C \sin\left(\Lambda_E + \lambda\right) & \cos\left(\Lambda_E + \lambda\right) & -\cos\phi_C \sin\left(\Lambda_E + \lambda\right) \\ \cos\phi_C & 0 & -\sin\phi_C \end{bmatrix} \tag{B53}$$

The transpose of either $\left[T_{G2I}\right]$ or $\left[T_{C2I}\right]$ is denoted by a tilde.

APPENDIX C

STUDIES TO DETERMINE ANGLE-OF-ATTACK EFFECTS

One assumption used in the past concerning angles of attack is still applicable to the updated techniques presented herein. This assumption says that a stable axisymmetric flight vehicle will fly at small angles of attack, and consequently, all aerodynamic force will be drag force. A preflight study was made to determine if this assumption was valid. Three areas where angle-of-attack effects could occur were investigated: (1) in the presence of gusts and winds, (2) following tipoff from the launch aircraft, and (3) encountering pitch-roll resonance phenomena.

In order to evaluate the effects of gusts and winds on the angle of attack, reference 7 was studied to understand the nature of winds. This reference stated that outside of the Earth's atmospheric boundary layer (above approximately 1830 m), in the absence of any frontal or local storm activity, and within time periods of up to as long as an hour, winds are steady and uniform and have no vertical components. However, there are wind shears that, when penetrated by aircraft or missiles, appear to an observer in the aircraft to be gusts as one would think of them on the surface of the Earth. But, in fact, there would be virtually no gusts in the flight regime of interest. In order to study the response of the flight vehicle to the penetration of wind shears, a six-degree-of-freedom computer simulation was conducted. Worst-probable (3σ) wind-shear gradients $\left(\frac{\Delta V_w}{\Delta h} = 0.05 \frac{m/sec}{m}\right)$ were numerically superimposed on a statistical mean wind for Wallops Flight Center. (See fig. C1.) Also shown are vehicle altitude and angle-of-attack response time histories. These indicate that the vehicle weathercocks into the free-stream velocity vector and reaches a total angle of attack no greater than 0.45°. Therefore, the effects of "gusts" and wind upon the accuracy of the Mach number and drag coefficient are small. Since the six-degree-of-freedom simulation shows that the model reaches a small total angle of attack (0.45°) while penetrating 3σ wind shears, the assumption that the model will fly a zero-lift trajectory is reinforced.

Again using a six-degree-of-freedom program, a short study showed that tipoff of as much as 12° initial angle of attack would damp to acceptable values by the time the flight vehicle had reached the test region.

Another study using measured values of fin tip deflection and best engineering estimates of center-of-gravity offset were used in six-degree-of-freedom simulations to check for possible roll-resonance problems. None were found in the simulations and none were seriously expected in flight, for each model was mass balanced.

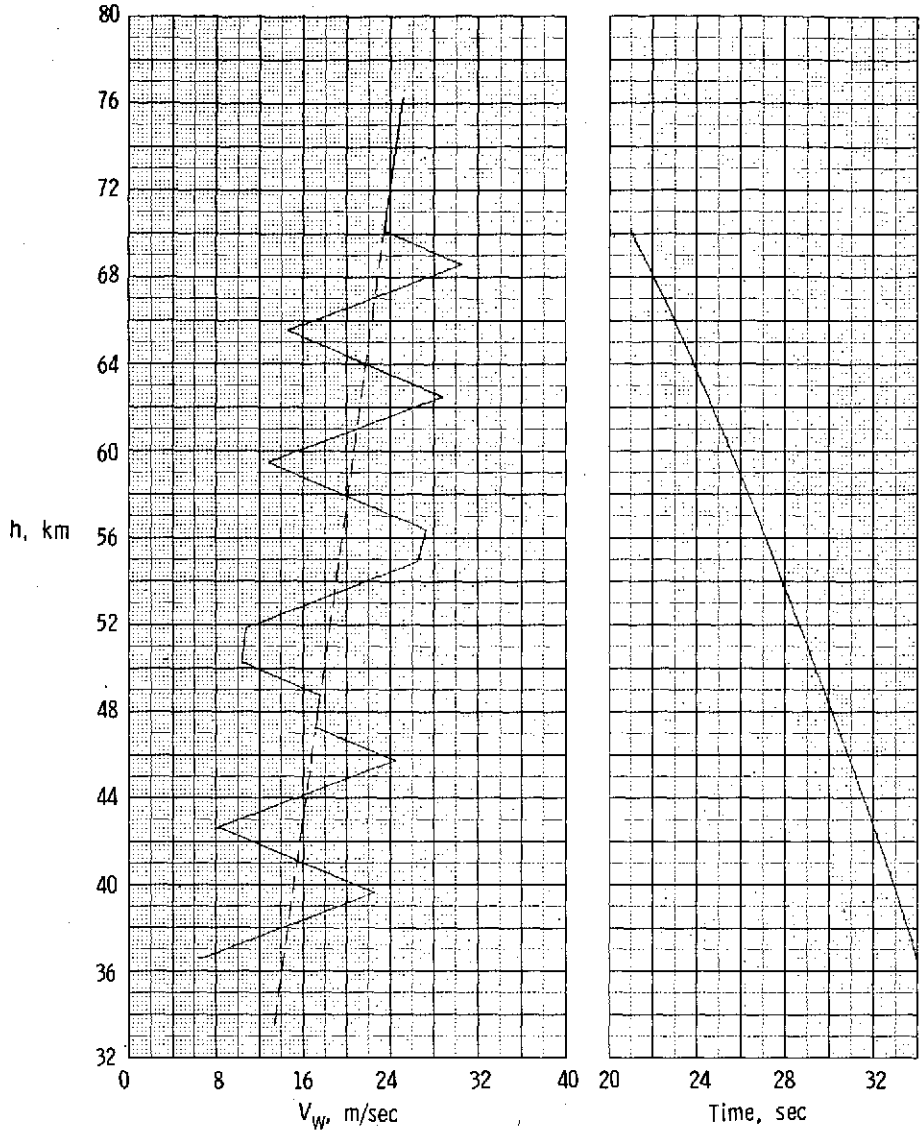

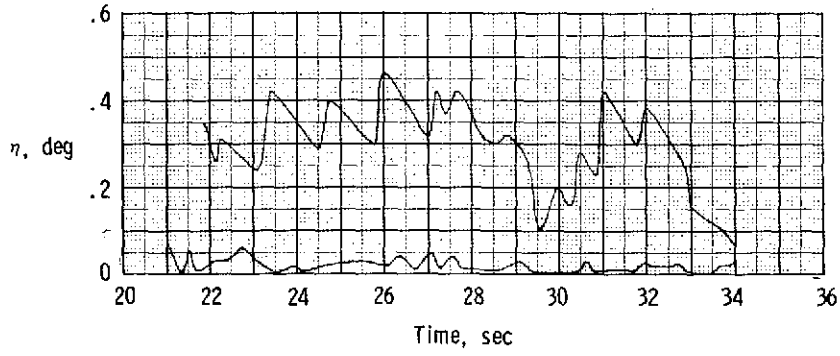

Figure C1.- Determination of angle-of-attack effects.

REFERENCES

1. Usry, J. W.; and Wallace, John W.: Drag of a Supercritical Body of Revolution in Free Flight at Transonic Speeds and Comparison With Wind-Tunnel Data. NASA TN D-6580, 1971.

2. Dennison, A. J.; and Butler, J. F.: Missile and Satellite Systems Program for the I.B.M. 7090. Tech. Inform. Ser. No. 61 SD 170, Missile and Space Vehicle Dep., Gen. Elec. Co., Feb. 1962.

3. Stoney, William E., Jr.: Collection of Zero-Lift Drag Data on Bodies of Revolution From Free-Flight Investigations. NASA TR R-100, 1961. (Supersedes NACA TN 4201.)

4. Smith, Robert E., Jr.; Price, Joseph M.; Howser, Lona M.: A Smoothing Algorithm Using Cubic Spline Functions. NASA TN D-7397, 1974.

5. Scoggins, James R.: Sphere Behavior and the Measurement of Wind Profiles. NASA TN D-3994, 1967.

6. Aldrich, G. T.; and Krabill, W. B.: A Versatile Kalman Technique for Aircraft or Missile State Estimation and Error Analysis Using Radar Tracking Data. AIAA Paper No. 72-838, Aug. 1972.

7. Henry, Robert M.; Brandon, George W.; Tolefson, Harold B.; and Lanford, Wade E.: The Smoke-Trail Method for Obtaining Detailed Measurements of the Vertical Wind Profile for Application to Missile-Dynamic-Response Problems. NASA TN D-976, 1961.